SECTION 1: LOCATION OF MAGNETISATION BY MAGNETIC FIELD INVERSION

This page intentionally left blank

2
Data selection and optimisation for magnetic field inversion

C.A. Foss

ABSTRACT

Magnetic field inversion is data-centric. In this chapter I explain how the capabilities and limitations of inversion depend on the input data, including data acquisition and processing. We do not invert the magnetic field – only samples of it, and those samples are subject to distortion as well as misrepresentation by sampling bias and limitation. Gridding in particular, is a major transformation of the primary measurements, generating apparent data where no measurements have been made. Inversion of gridded data should be performed only where necessary or with a thorough evaluation and justification.

The Earth's magnetic field combines the fields of multiple crustal magnetisations together with core and ionospheric contributions into a single field. One of the most challenging tasks of inversion is to ascribe measured magnetic field variations to selected magnetisations so that inversion can be performed on appropriate data. Field separation is interpretive, and we should not rely on inversion itself to perform that separation without careful supervision. It is only those parts of the magnetic field that dominate its local curvature that can be reliably inverted. These are generally field contributions from the shallower magnetisations.

2.1 INTRODUCTION

This chapter presents case studies to illustrate unconstrained magnetic field inversion. Reading through these examples will provide an understanding of how to select data appropriate for magnetic field inversions and how to design inversions to achieve a required output. For successful inversion the magnetic field must include distinct features that can be attributed to distinct magnetisations. This restriction is not because less distinct field variations cannot be inverted but because without distinctive features ambiguity severely restricts the value of any inversion results and those results might well be misleading.

A common misconception is that inversion is an output model-focussed process in which data play only a passive role. A more holistic view is that inversion is data-centric with output models as advanced analytic data products. Clearly inversion can only be expected to return a justified model of subsurface property distribution if the input data are valid and sufficient. Input of reliable data to an inversion requires attention throughout acquisition and processing and those operations should be documented with comprehensive metadata. Incorrect assumptions about data units, geolocation and what processing has been applied to data are common and avoidable causes of invalid inversion results. Statistical checks should be performed to ensure that all data values are in expected ranges and those numerical error traps should be complemented with visual inspection of the data to rapidly reveal data flaws that if overlooked might invalidate inversion results. An inversion which reveals a flaw in the input data is wasted time and effort.

2.2 SURVEY PLANNING

Exploration geophysics is task oriented. Surveys are undertaken as a cost-effective means to support decision-making in a project. The decision to run a survey and the design of that survey are informed by consideration of the project objectives. Important survey design decisions cover survey extent, instrumentation, measurement spacings and, in the case of airborne surveys, line direction and terrain clearance. A key paper by Reid (1980) provides rules of thumb about line spacings required for subsequent analysis of magnetic field data and a free E-book by Colin Reeves (2005) provides an excellent review of the aeromagnetic method. Synthetic data modelling has a role to play in survey design such as optimisation of flightline spacing and/or flying height. Decisions made in survey planning, data acquisition and processing determine the capabilities and limitations of subsequent inversions and possibly the success of the project.

2.3 NETWORK ADJUSTMENT OF MAGNETIC SURVEY DATA

A common process applied in airborne surveys is to fly tie-lines perpendicular to the flightlines at a spacing of five to ten times the flightline spacing. A network adjustment is then applied to minimise residual differences at each tie-line and flightline intersection. This empirical process is critical to ensure data quality but there should be concern if tie-line levelling significantly changes the data. Data commonly available from aeromagnetic surveys may include 'raw' magnetics without diurnal correction, and the subsequent processing product of 'tie-line-levelled' magnetics includes diurnal correction, removal of heading errors and network adjustment. Neither data channel is ideal for inversion. 'Raw magnetics' includes unwanted noise and for the tie-line-levelled data there is no longer an appropriate elevation channel because network adjustment includes adjustments to accommodate elevation differences between flightlines and tie-lines without providing a new elevation reference for the magnetic data. Nevertheless, tie-line-levelled data is generally the preferrable data channel for inversion. Elevation inconsistencies between flightlines and tie-lines and between adjacent flightlines are most problematic in areas of rugged terrain. These problems should be anticipated in survey planning and reduced by flying a smooth drape survey focussed primarily on flying lines within a smooth envelope above terrain rather than honouring a constant ground clearance.

Tie-line levelling is commonly followed by micro-levelling to attenuate residual artefacts which would otherwise have prominent expression in subsequent grid enhancements such as vertical gradient computation. Micro-levelling uses a combination of directional and wavenumber filtering designed to preferentially attenuate field variations parallel to the flight direction and related to the line spacing (Minty 1991). Micro-levelling, however, has low discrimination and reduces the amplitude of many true field variations. Micro-levelling significantly modifies more problematic data. Remedial reprocessing designed to correct those problems as far as possible is a better option. Micro-levelled grids are less suitable than tie-line-levelled grids for quantitative applications such as inversion. It is also a common practice to resample the micro-levelled grid back onto line data, but again it is preferrable to invert the tie-line levelled channel in which levelling artefacts may be evident, rather than the micro-levelled channel where they have been cosmetically supressed possibly modifying the signal of interest.

2.4 IMPORTANCE OF DATA VISUALISATION

Isles and Rankin (2013) review the expression of geological features and structure in magnetic field imagery and this geological basis is crucial for informed inversion of magnetic field variations due to geology. Data visualisation is of critical importance in magnetic field inversion and supports the understanding required to make decisions about its inversion and interpretation. Images should convey the true amplitude of features. These amplitudes are obscured in histogram equalisation but can be restored by overlaying the images with contours. Addition of shadows and highlights in image sun-shading emphasises the expression of features which may be valid and of interpretational importance but which may not have sufficient amplitude for meaningful inversion. All inversions should be preceded by careful visual inspection of the input data, and no inversion results should be accepted until the computed field of the output model has been visually inspected.

Figure 2.1 shows a TMI image over a region near Echuca in Victoria derived from a survey with east–west flightlines at 400 m spacing and nominal terrain clearance of 100 m. The image shows a string of discrete, well separated and slightly elongate anomalies. On cursory

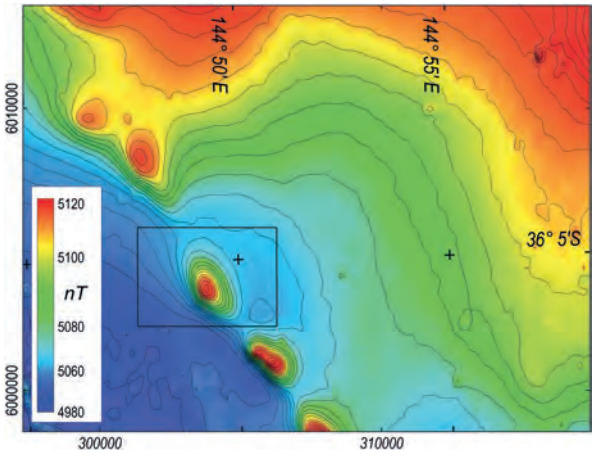

Fig. 2.1. TMI image over a string of magnetic bodies near Echuca, Victoria.

inspection of the anomaly in the inset area of Fig. 2.1 it seems that a simple model may be most appropriate for its inversion. The source magnetisation is interpreted to be a steeply plunging pod (possibly associated with a sub-vertical fault) truncated at the top of basement beneath a younger cover. This anomaly is shown in more detail in Fig. 2.2. An elliptic-section horizontal-top cylinder seems suitable to represent the magnetisation with sufficient versatility and an appropriate level of detail. The background field on which the anomaly is superimposed has a gentle gradient from north-west to south-east and for the modelling is represented by an almost planar surface of that trend. The external magnetic field of a geological body is an expression of its resultant magnetisation – the vector sum of its induced and remanent magnetisations. For anomalies such as those shown in Fig. 2.1 which by visual inspection seem consistent with magnetisation in the geomagnetic field direction, source magnetisation can initially be assigned to be induced only. Alternatively, these well-separated, well-defined anomalies also allow the magnetisation to be assigned as including remanence of unknown direction. For simplicity in this study I use an induced-only magnetisation assumption to generate one possible model of the magnetisation. I positioned a pipe body with elliptical section and horizontal-top surface beneath the anomaly and gave it an initial test susceptibility. I then adjusted susceptibility and top depth of the model using a few trial computations to produce a suitable starting model for inversion. I ran the inversion with free horizontal position, depth to top, elliptic axial section radii and azimuth, depth extent and magnetic susceptibility. The resulting best-fit inversion model has a depth below surface of 720 m, length 2130 m,

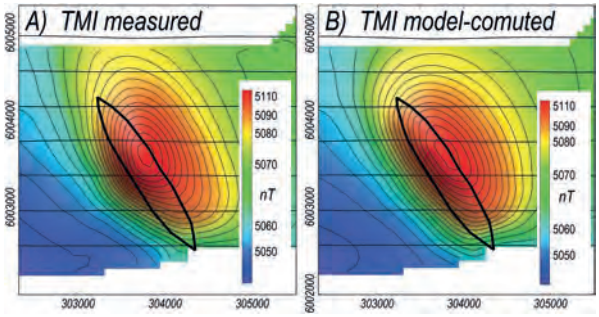

Fig. 2.2. A) measured and B) model computed TMI over the anomaly highlighted in Fig. 2.3. The outline of the top surface of the inversion body is plotted over the images.

maximum width 340 m, and magnetic susceptibility 0.024 SI. Images of the input measured and inversion-model computed fields are shown in Fig. 2.2. The model field is the combination of the proposed regional field and the proposed anomalous model field. The two images in Figs 2.2A and 2.2B show a strong but imperfect match, suggesting that the model is a candidate representation of the magnetisation.

Figure 2.3A shows stacked profiles of the measured, model-computed and regional fields. This display provides greater discrimination of the match between observed and computed fields and reveals systematic line-to-line displacements between them suggesting that the model would benefit from additional complexity to reduce this misfit. I replaced the initial elliptic section pipe with a polygonal section pipe which I subsequently inverted allowing individual horizontal displacement of the vertices. The other model parameters were also free to adjust their best values to optimise for this new model type. A plan view of the top of this more complex inversion model with its stacked profiles is shown in Fig. 2.3B. The data misfit shown by the stacked

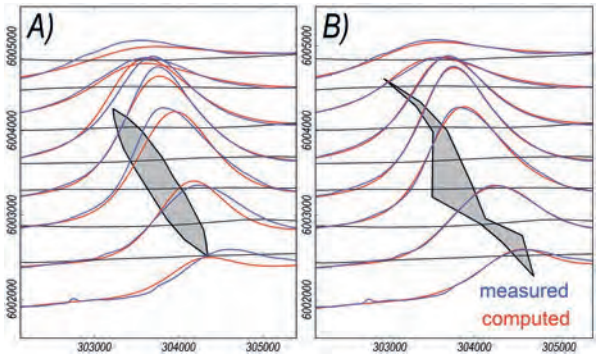

Fig. 2.3. Stacked profiles of measured and model computed TMI over A) the elliptic section pipe model and B) the polygonal section pipe model.

profiles in Fig. 2.3A is considerably reduced by the more complex model that has a depth below surface of 520 m, length 2950 m, width 450 m, and magnetic susceptibility 0.024 SI. These statistics are not substantially different to those of the elliptic pipe model, but due to improved fit to the data the more complex polygon section model shown in perspective view in Fig. 2.4 is (quite subjectively) considered a superior representation of the subsurface magnetisation.

Figure 2.5 shows a plot of the top of the model outline over an image of the tilt of TMI. The tilt is the ratio of vertical and horizontal derivatives of the field (Miller and Singh 1994) with units of degrees. With only indirect expression of field amplitude this enhancement is not well suited as input to inversion but the match between the image and the model section provides visual support for the additional model complexity. Data visualisation played a significant role in the development and acceptance of this inversion model.

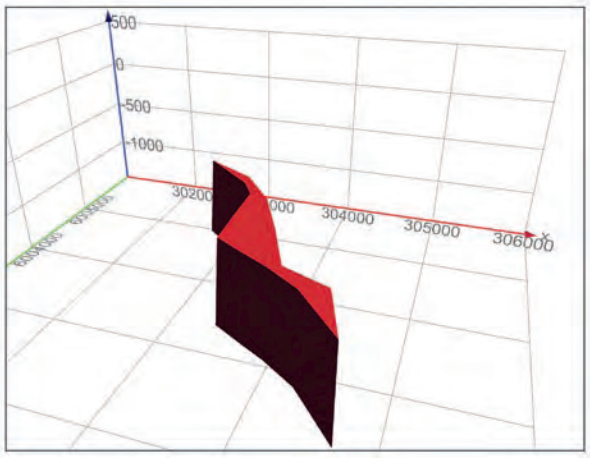

Fig. 2.4. Perspective view of the polygonal section pipe model.

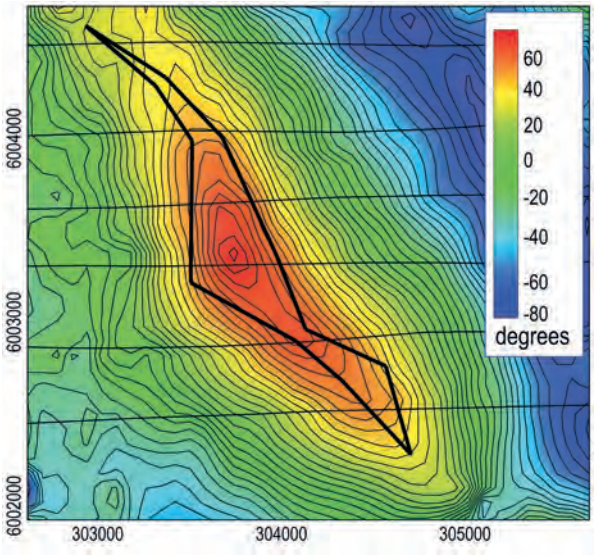

Fig. 2.5. Plan of the top surface of the polygonal pipe model over TMI tilt image.

2.5 DATA FOCUS AND SEPARATION OF FIELDS TO BE INVERTED

In inversion it is important to optimise the expression and detection of differences between measured and model computed fields and thereby narrow the range of acceptable models. With increasing computer power and speed ever-larger inversion models are being run – necessarily diluting their focus. A superior strategy is 'divide and conquer' by isolating individual features in the magnetic field data and restricting the data used to be only that required to invert for each feature separately. In many areas only a small proportion of the magnetic field carries source-diagnostic information and little is lost in excluding the remaining data. Figure 2.6 shows an image of TMI over an area near Brewarrina in New South Wales. In this image all the information that can support meaningful inversion of the subsurface magnetisation occurs within less than 10% of the area. The most effective inversion of the data is to focus on each anomaly in turn using data clips as the one shown in Fig. 2.6 that isolates data for two immediately adjacent anomalies. The overlap between these anomalies prevents their reliable individual inversion. The anomalies are defined by survey data on east–west flightlines at 400 m spacing and nominal terrain clearance 80 m flown for the New South Wales Geological Survey to promote mineral exploration. Another five or

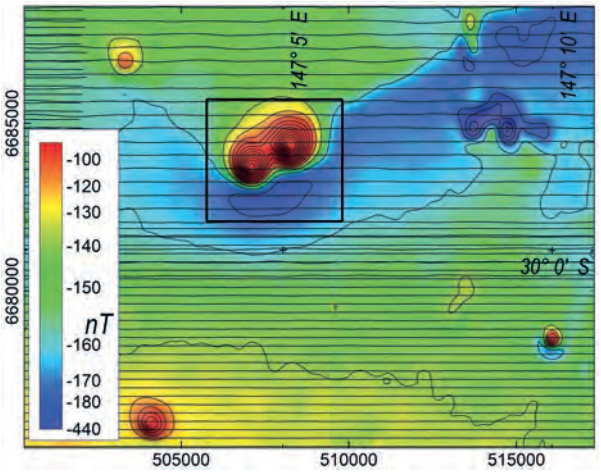

Fig. 2.6. TMI image of two overlapping magnetic pipe anomalies near Brewarrina, New South Wales.

six data clips could be applied to the data imaged in Fig. 2.6 to investigate other discrete anomalies.

Once data selection is optimised the next task is to separate that part of the field variation that is to be explained by the inversion model. This separation is best performed before inversion so that inversion begins with a suitable starting model, thereby improving chances of convergence to an acceptable solution. There are many proposed methods of regional-residual separation to isolate an anomaly from its background field but no method is automatically justified. Regional and residual fields need not conform to any analytic definition and are not better qualified if they do. Spectral separation of fields rarely achieves the degree of separation ideal for inversion because regional and residual field spectra overlap. A method of regional-residual separation by Li and Oldenburg (1998) performs an inversion across a wider zone around the area of interest to define the regional field. This method may work well for some anomalies but lacks the flexibility to be optimised by human guidance.

Regional-residual separation is so critical to an inversion that no automated method should be trusted to make this separation unsupervised. Field separation is fundamentally interpretive and visual inspection of both the regional and residual fields is an important quality control operation before submitting the residual data for inversion. As an inversion proceeds it may become evident that a different separation might be more appropriate, in which case it is quite acceptable to interrupt the inversion and adjust the separation. Adjustments of the anomaly separation are most commonly required for inversion of deep-going magnetisations for which fields of the modelled magnetisation extend considerable distances with only gradual transition to the background field. For bodies of shallow depth extent the transition from the anomaly to the surrounding background field is generally sharper and closer to the margin of the magnetisation. If it is not possible to reliably separate background and residual fields before an inversion is started then it is unlikely that the inversion itself will supply a meaningful solution, although inversion can be used to make modest adjustments to the regional. Multiple inversions using different regionals may be required for particularly problematic regional-residual separations to test the consequences of that uncertainty.

The overlapping anomalies in the data-clip area of Fig. 2.6 are proposed to be due to adjacent intrusive pipes truncated at the top of a weakly magnetised crystalline basement beneath an unknown thickness of non-magnetic cover. An appropriate model geometry for this interpretation is a pair of vertical or steeply plunging circular or elliptic section cylinders with horizontal top surfaces (similar to the initial model used in the previous Echuca case study). Anomaly separation was straightforward in the Echuca case because of the very different characteristics of the regional and residual fields. That is also the case for the isolated anomalies in the Brewarrina area as shown in Fig. 2.6 but anomaly separation between the fields of the two pipes themselves is more problematic and neither anomaly can be reliably inverted alone without resolving the overlapping field of the other. The degree of overlap is highlighted in the three-dimensional display of the TMI anomalies shown in Fig. 2.7. The anomalies in a two-dimensional FFT vertical derivative transform of the TMI data also shown in Fig. 2.7 have significantly reduced overlap and independent inversion of each anomaly would be assisted by inversion of the derivative rather than the TMI data. However, I decided to simultaneously invert the two TMI anomalies using a two-body model.

As shown in Fig. 2.6, the anomalies are predominantly positive with a weak negative to the south as generally expected for bodies of induced magnetisation at this geomagnetic inclination. However, the two anomalies to the south-west in Fig. 2.6 are both positive-only and nearby there are similar anomalies of negative polarity, suggesting that remanent magnetisation of alternate polarities is significant for this population of bodies. For these compact, sufficiently sampled anomalies there is little reason other than their overlap not to invert for both magnetisation direction and the spatial distribution of magnetisation and I chose this option. If the magnetisation is parallel to the local geomagnetic field then the magnetisation direction recovered by the inversion should be that of the local geomagnetic field, with the advantage that magnetisation direction has

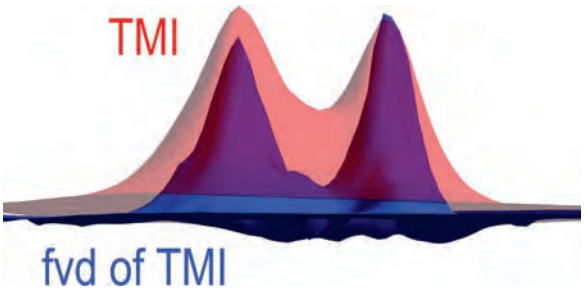

Fig. 2.7. Three-dimensional display of overlapping anomalies of TMI (red) and vertical derivative pf TMI (blue).

been tested rather than assumed. Without independent information only the resultant magnetisation can be recovered from a static magnetic field anomaly. In this study I arbitrarily assigned all magnetisation to be remanent but gave it an initial direction parallel to the geomagnetic field.

I generated a starting mode for inversion by placing a vertical cylinder with magnetisation in the local geomagnetic field direction directly beneath each of the two anomalies and adjusted their depth and magnetisation intensity to approximately match the measured anomalies. From this starting model I ran an inversion with free horizontal position, depth to top, depth extent, cross-section radii and azimuth, axial plunge and plunge azimuth, and magnetisation intensity and direction for each body. A further advantage of working with a small data subset cut to just beyond the extent of the anomalies is that the inversions proceeded rapidly, even with many iterations to investigate the 24-dimensional model space. Success of the inversions was encouraged by having a reasonable starting model and small bounds ranges forcing multiple iterations in small steps within the parameter space rather than large and possibly unstable jumps. Figure 2.8 shows the post-inversion bodies beneath the TMI anomalies and Fig. 2.9 shows stacked profiles of the input measured field, regional field, and output computed field.

The concern of simultaneously inverting for two source bodies is that each body may in part explain field variation due to the other. Both non-vertical plunge and magnetisation direction of these deep-going bodies can

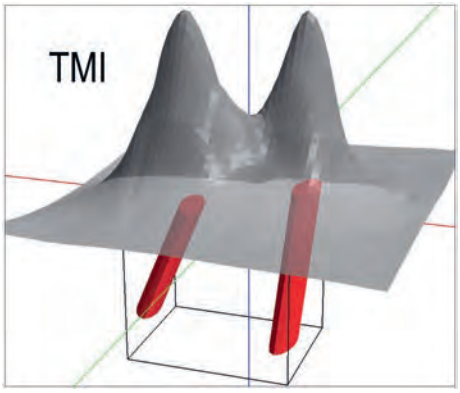

Fig. 2.8. 3D display of the TMI anomalies over the inversion source model.

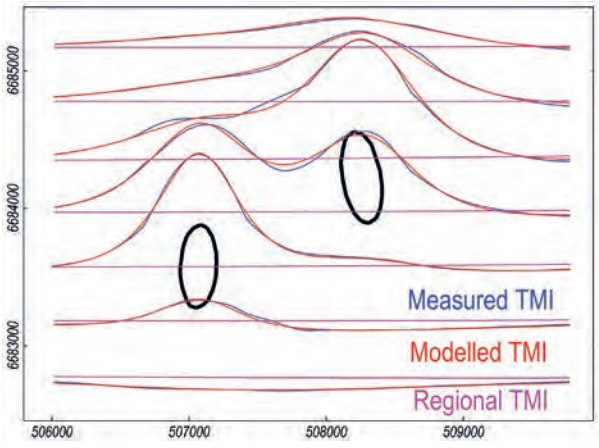

Fig. 2.9. Flightlines and stacked profiles of the measured (blue), regional (magenta), and model-computed (red) fields due to the model of two elliptic pipes.

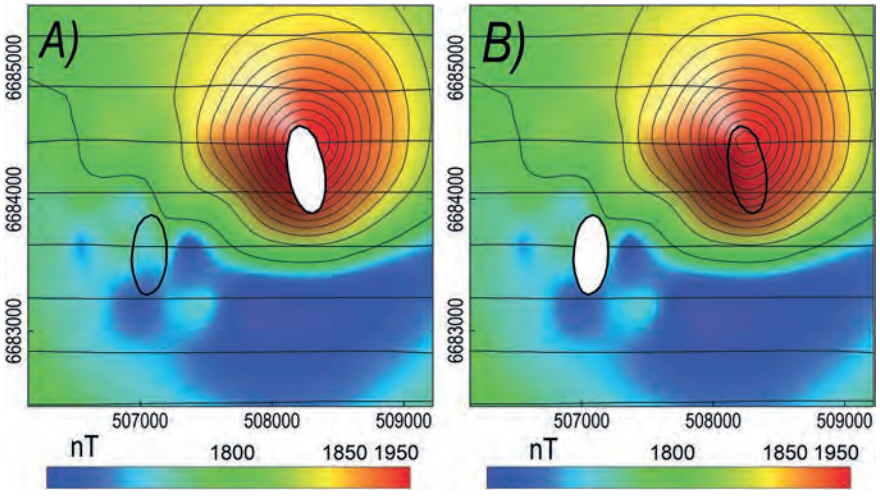

Fig. 2.10. A) and B) Images of fields generated by subtracting from measured TMI the fields computed from the individual inversion model bodies. In the combined inversion each body performs the task of explaining a single anomaly.

adjust to explain asymmetry in their anomalies and this provides opportunity for either body to incorrectly explain a part of the adjacent anomaly. However, an appropriate starting model reduces this opportunity. To illustrate how effectively each body explains only its own anomaly despite the opportunity to do otherwise, Fig. 2.10 shows the fields computed by subtraction of the individual computed body fields from the measured TMI. In each case there is no residual indication of the anomaly due to the subtracted body as would be seen for cross-contribution between the model bodies and anomalies. The model also has acceptable internal consistency, with an angular difference of only 6° both between the plunge of the two bodies and also between their magnetisation directions.

This study highlights the advantage of inversions designed to link specific field variations to their interpreted sources. The decisions to be made require understanding the geology and recognition of any diagnostic characteristics of the field, generally from visual inspection of the data. Without this guidance it is less likely that an inversion will produce a sensible result. It is reassuring that from this starting model the guided inversion resulted in each model body performing its allocated task.

2.6 SEPARATION OF ANOMALIES FROM A STEEP REGIONAL GRADIENT

In each of the previous case studies the regional gradient across the extent of the anomalies causes much smaller field variation than the residual anomaly to be inverted. Figure 2.11 shows examples where anomalies are superimposed on steep background gradients that cause field variations with significant amplitude compared to the residual anomalous field. In these cases correct estimation and treatment of the regional field is particularly critical to the success of the inversion.

Figure 2.11 is an image from a heli-mag survey over the Rylstone area of New South Wales, flown on east–west flightlines with a nominal terrain clearance of 50 m. The Rylstone area contains many intrusive and

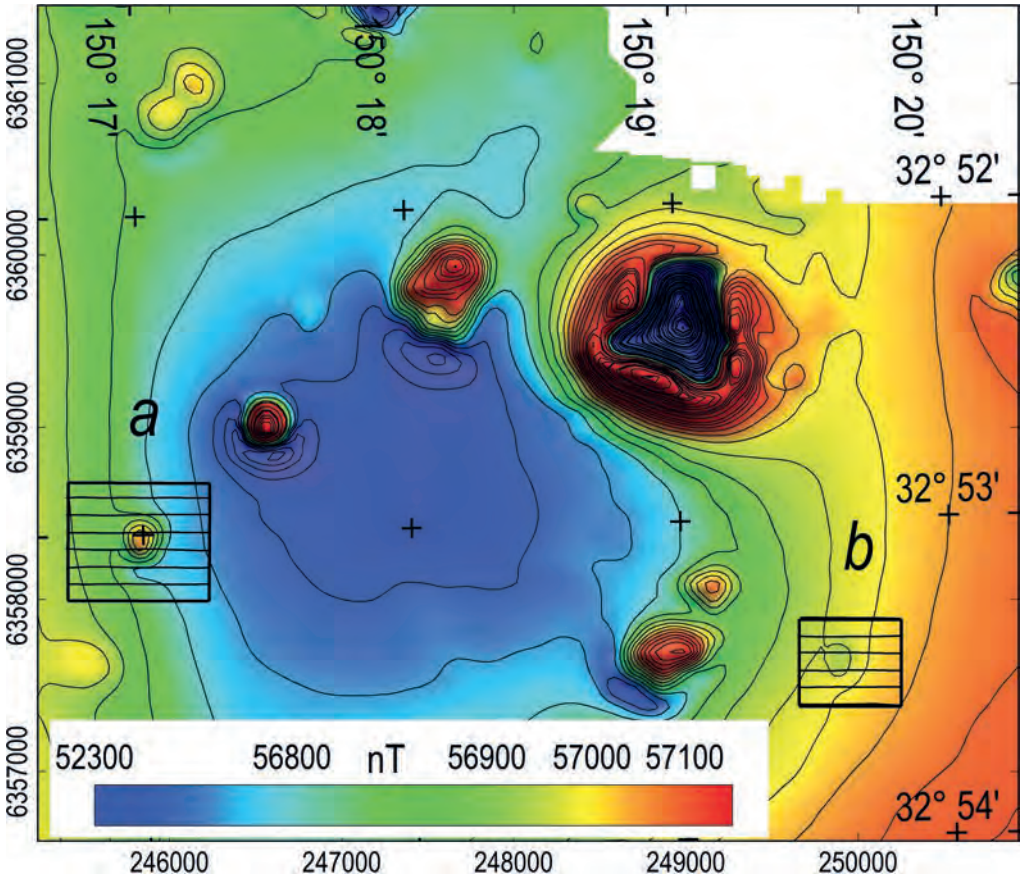

Fig. 2.11. TMI of an area near Rylstone with two anomalies 'a' and 'b' superimposed on steep background gradients.

volcanic bodies of different ages, many with prominent remanent magnetisation. The anomalies 'a' and 'b' in Fig. 2.5 (Australian Remanent Anomalies Database anomalies 319 and 320) are believed to be narrow Tertiary-age pipes with dominant normal and reverse remanent magnetisation respectively. Figures 2.12 and 2.13 show model sections on flightlines through the centres of the anomalies (each is the centre line from a seven-line inversion). For the predominantly positive anomaly 'a' the regional field variation and the peak residual anomaly amplitude are both ~120 nT. For anomaly 'b' the regional field variation is of the order of 80 nT and the central anomaly trough amplitude is 50 nT. The model sections show that on the centre lines for both anomalies the regional field is well represented as a near-linear gradient. The anomalies are both well matched by addition to the regional field of anomalous fields derived by inversion of horizontal-top, elliptic-section, remanently magnetised cylindrical bodies.

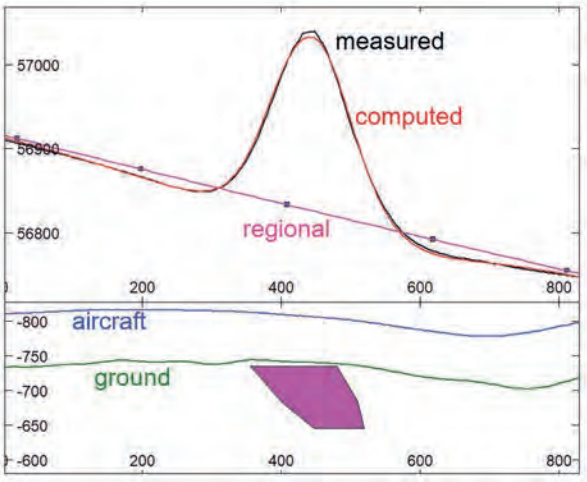

Fig. 2.12. Central flightline section for anomaly 'a'.

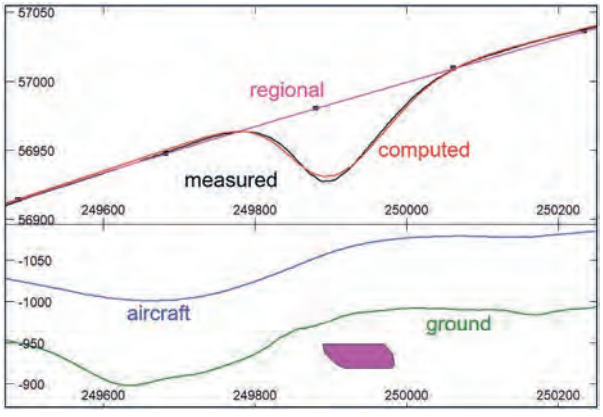

Fig. 2.13. Central flightline section for anomaly 'b'.

The positive anomaly 'a' is imaged in Fig. 2.14A. The anomaly is strongly asymmetric in the direction of the regional gradient with the contours compressed to the side of the anomaly where regional and anomaly gradients reinforce and are drawn apart on the side where the two gradients are in opposition. The regional field is computed as a second-order polynomial from all model lines but is almost planar as imaged in Fig. 2.15 A. The residual field derived by grid subtraction of the regional field from the measured TMI is imaged in Fig. 2.15B. There is no indication in either image of contamination by the other field component, suggesting that the regional-residual separation is highly effective with the appropriate residual field submitted to the inversion. The negative anomaly 'b' as shown in Fig. 2.14B has a smaller amplitude in comparison to the regional gradient across it and is expressed primarily as a deflection of the regional field contours. The regional and residual separations for this anomaly are shown in Fig. 2.16 A and B respectively, again with very effective separation between the fields.

These results establish the feasibility of performing inversion in the presence of a dominant regional field gradient. However, these are not the most challenging cases of regional-residual separation. Although the regional gradients are strong they are almost planar, easily predictable from the surrounding data, and with a substantial contrast in curvature between the regional and residual fields. More challenging separations arise when these conditions are not met and a residual field to be inverted has to be separated from a regional field of similar curvature, or where the anomaly is close to the edge of a survey where some of the data required to define the regional field are unavailable.

2.7 THE INFLUENCE OF DATA SPACING

Input data to an inversion must be not only valid but also of sufficient precision, sample spacing and extent to reliably represent spatial variations in the magnetic field. Using spectral analysis, Reid (1980) suggested data spacing limits beyond which the magnetic field is unacceptably aliased and these have long been adopted as guidelines for survey planning. Reid's recommendations were that TMI surveys should use a flightline spacing no wider than twice the height above the shallowest magnetisation, that gradient surveys require a line spacing at one-half of that

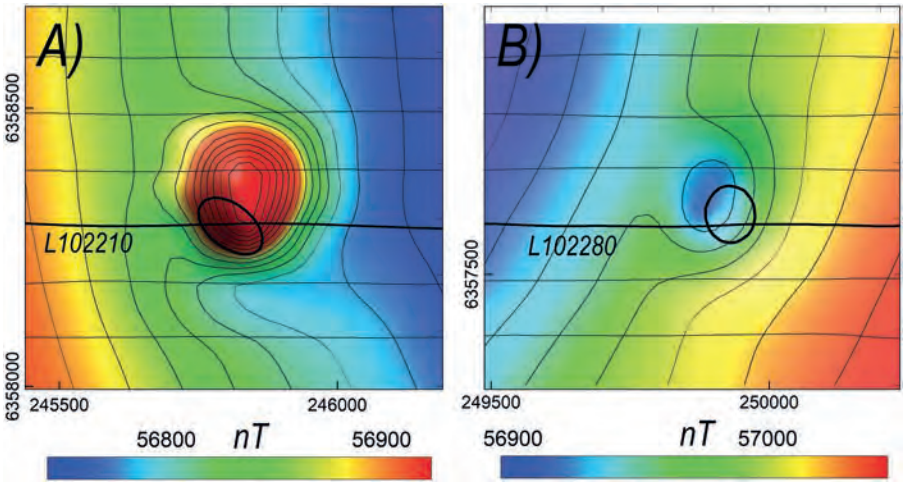

Fig. 2.14. Measured TMI anomalies 'a' and 'b' with outlines of the model top surfaces.

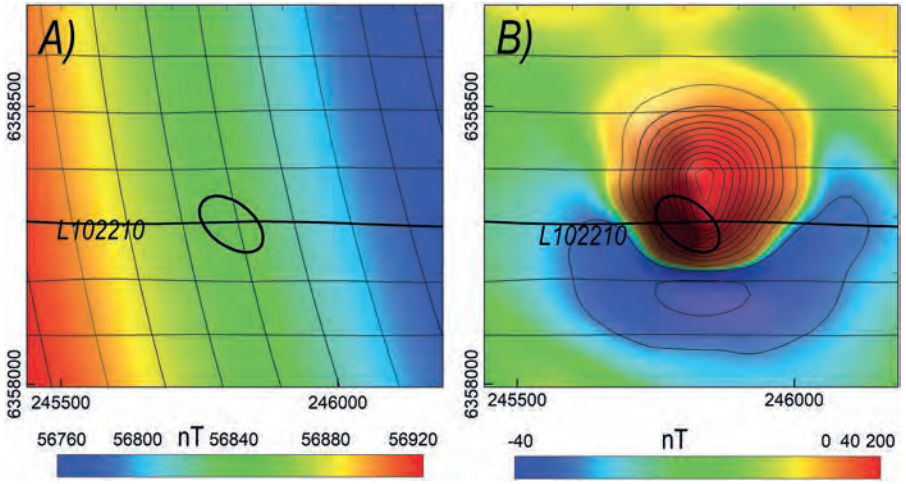

Fig. 2.15. A) regional and B) residual TMI separations for anomaly 'a'.

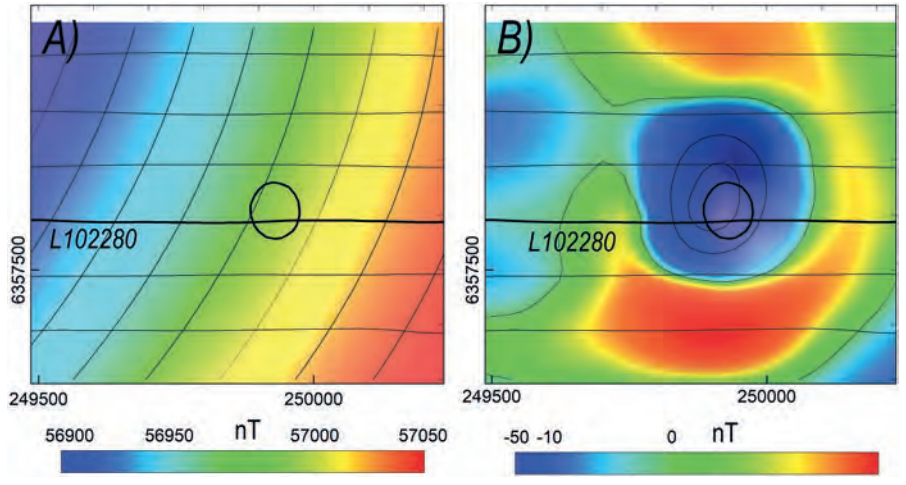

Fig. 2.16. A) regional and B) residual TMI separations for anomaly 'b'.

limit and that surveys designed to collect data for modelling or inversion should use a line spacing no wider than half the height above the top of magnetisation. These limits avoid substantial aliasing but it may well be of advantage to further increase sample density and provide additional resolution and fidelity of the mapped field and its gradients beyond minimum requirements. Consistent with Reid's analysis, mapping of short wavelength field variations near a source requires closer sample spacing and higher spatial precision than measurement of the longer-wavelength distant parts of the field.

Inversion optimises a model not to matching of the magnetic field but to matching the specific sample of the field that is submitted to it. Even with high-quality data, if those data do not sufficiently sample the field, do not extend sufficiently, or are at too high an elevation above the magnetisation there can be substantial challenges in mapping the magnetisation.

To illustrate linkage between data sampling and inversion results I present an example of gravity and magnetic surveys over the Waukarlycarly Graben and surrounding shallow Proterozoic basement of the Paterson region on the western edge of the Canning Basin in Western Australia as located in Fig. 2.17. The geology of the area is described by Alavi (2013) and the data inversions are from Foss and Purcell (2006). The gravity low over the area is interpreted as due to an accumulation of sediments, interpreted to have started with a rifting episode in the early Cambrian and to have been reactivated through to the Permian. A single seismic line traverses the main gravity anomaly with a reflection interpreted as acoustic basement at 1.7 to 1.8 s two-way time (2.3 to 2.5 km depth depending on the velocity estimates). There are several shallower

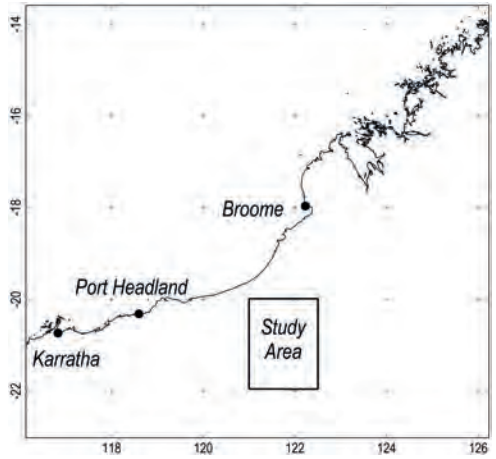

Fig. 2.17. Location of the Waukarlycarly study area.

sub-horizontal and fault-disrupted events but with no borehole control these are not confidently attributed to specific stratigraphic surfaces.

2.7.1 Gravity modelling and inversion

Figure 2.18A shows the gravity image of the area from previous sparse measurements, predominantly from stations at an 11 km spacing. The rules from Reid (1980) are not directly relevant for these data where the density contrasts extend almost to surface but the general principles of the need for sufficient data coverage still apply. A likely explanation of the observed elongate gravity low of up to 400 μm/sec^2 is variation in depth to the Proterozoic basement although the sparse data could also be matched by an intra-basement density low. Figure 2.18B shows a gravity image from a survey with a station spacing of 2.5 km, which is an increase in station density by a factor of almost 20. The sharp linear and parallel gradients of the gravity low defined by these higher-resolution data clearly suggest that the gravity low is due to a graben with sub-vertical faulted margins because these sharp gradients cannot be matched with a deep-going intra-basement density contrast. To enhance the gravity data I applied a two-dimensional FFT vertical derivative filter to the Bouguer grids to give the images shown in Fig. 2.19. Minimum curvature gridding of such sparse data introduces image artefacts in the form of 'pimples' at the location of each station. To supress these artefacts I preconditioned the data with a 500 m upward continuation before applying the gradient filter. This preconditioning has the advantage that it can be directly addressed in subsequent modelling and inversion by a corresponding increase in elevation of the computations. The vertical gradient filter accentuates expression of the graben that is the shallowest density contrast, but as noted by Reid (1980) a closer data spacing is required not just for gradient surveys but also to be able to effectively image gradients from transforms of field data. Gradient enhancement of the previous data (Fig. 2.19A) reveals the shape and extent of the gravity low more clearly than does the Bouguer gravity image but it is not clear that it is due to a fault-bounded graben. Gradient enhancement of the new data with the same 500 m upward continuation preconditioning shown in Fig. 2.19B is much more revealing, with substantial benefit from the increased data density. Enhancement of the higher resolution data provides convincing support for the gravity anomaly being due to a graben, with the sharp gravity variation over the fault margins tightly constrained by the data. Detailed inspection of the gravity and gravity gradient images of the

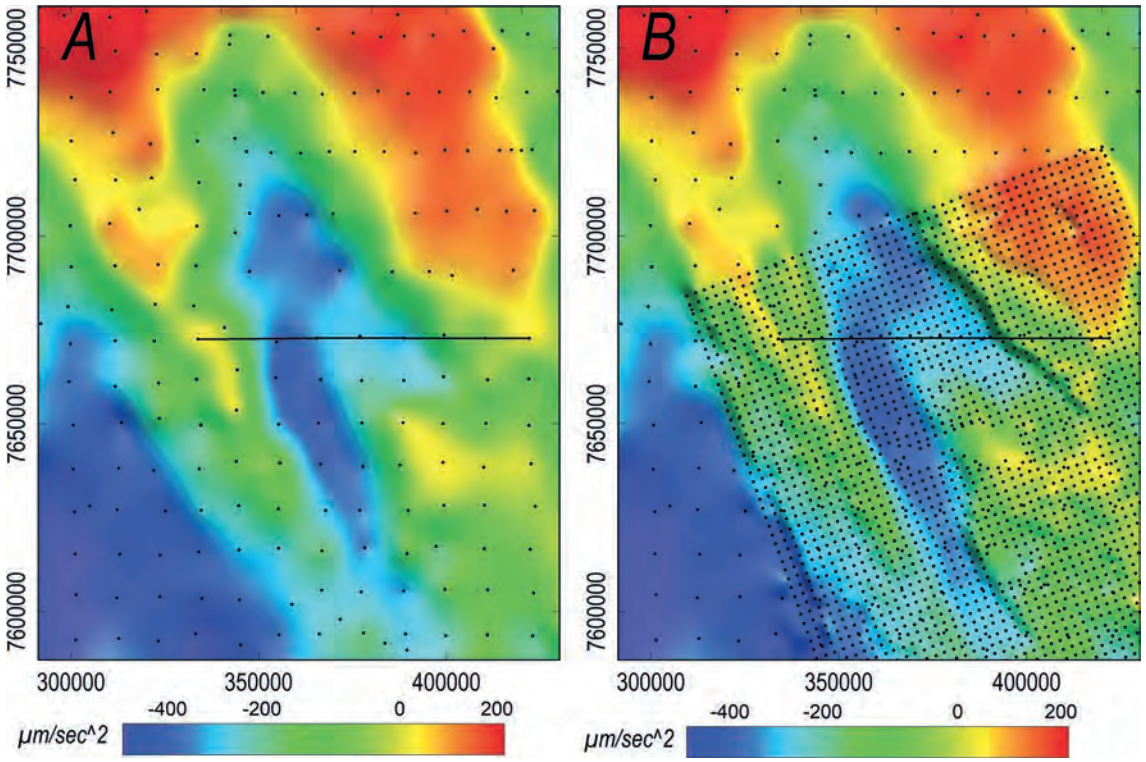

Fig. 2.18. Bouguer gravity images from gridding of A) previous sparse data and B) new closer-spaced data.

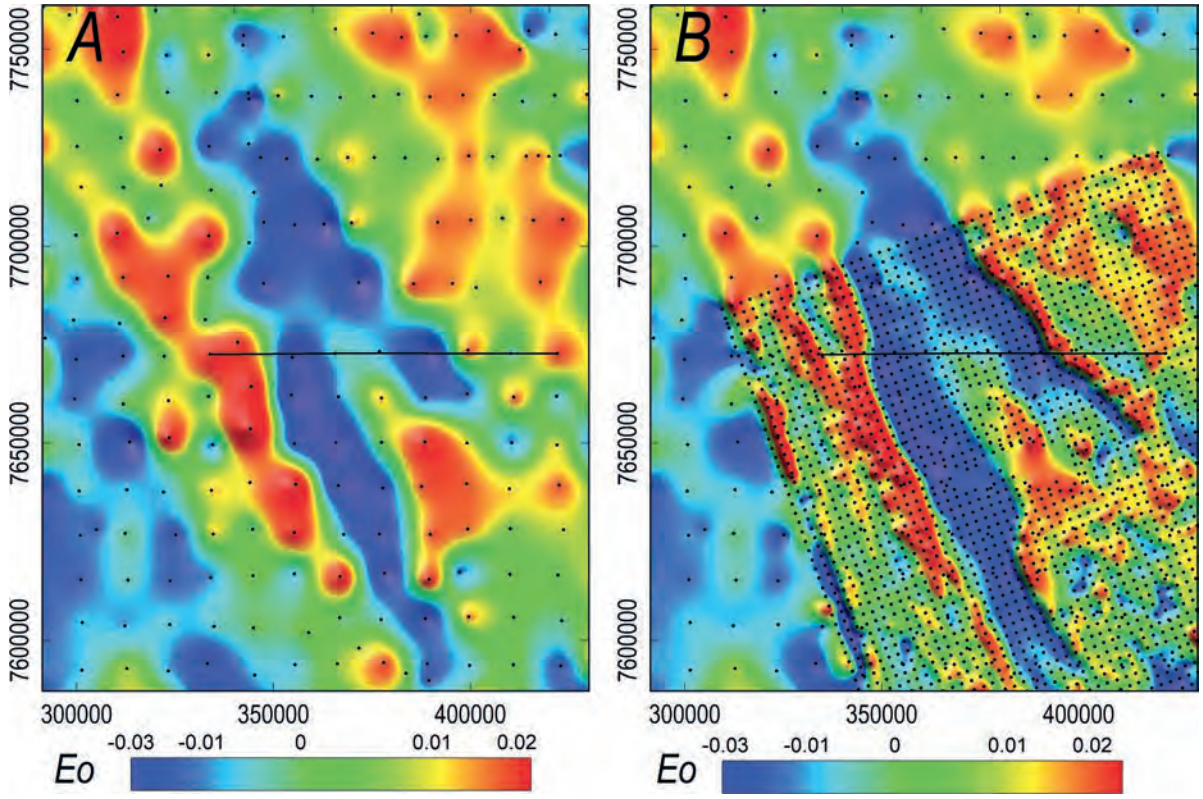

Fig. 2.19. Vertical derivative of Bouguer gravity from gridding of A) previous sparse data and B) new closer-spaced data.

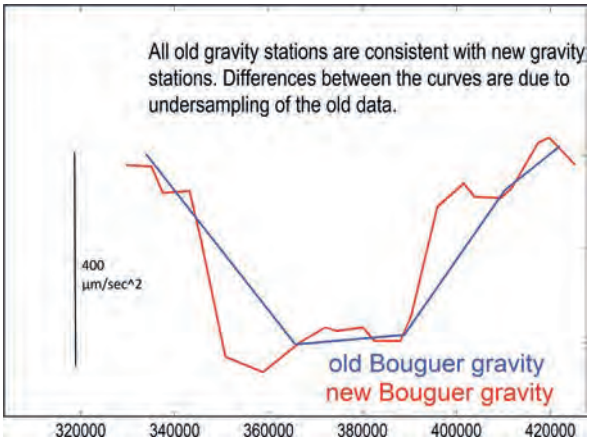

Fig. 2.20. Co-located profiles of previous (blue) and new (red) survey Bouguer gravity.

higher-resolution data in Figs 2.18B and 2.19B suggest that the graben is in fact two opposite and outward-facing half-grabens with an intervening central basement high (see also Alavi 2013).

A traverse across the basin is shown in Fig. 2.20. The previous data traverse contains only five stations and provides an insufficient mapping of the gravity field variation to confidently discriminate between different source models. The new data traverse contains 20 stations and localises the abrupt changes in gravity that are distinctive of the bounding sub-vertical faulted margins of the graben. The previous gravity data are of low quality by today's standards with pre-GPS positioning provided by feature recognition on aerial photography and elevation control by barometric altimeter. Nevertheless, these previous gravity stations are individually consistent with the new data. The weakness of the previous gravity coverage is the small number of stations and their wide spacing.

Once the initial interpretation has been made that the negative gravity anomaly is due to a graben, the gravity modelling and inversion depends substantially on the density contrast applied between the basement and graben fill. There are low amplitude circular and elliptic negative gravity anomalies over granites or granitoids in nearby shallow basement and using these as a best density estimate (because granites are composed mostly of minerals with similar densities to produce a reasonably predictable rock density) I selected a density of 2700 kg/m^3 to represent the basement. For the Palaeozoic graben sediments I selected a density of 2400 kg/m3 to give a density contrast of 300 kg/m3. The basin fill is expected to consist mostly of clastic sediments and even if these are uniform, their density will vary with depth due to compaction. Substantial density variations within the basin can also occur at major unconformities between different age sediments or if there are thick units of limestone, dolomite or salt (none of which are known to be present in this case). The underlying and surrounding basement is also inhomogeneous and may have density variations across large volumes. Despite this, there is little or no justification for a density model more sophisticated than a uniform contrast between basement and basin infill. Because steep density interfaces extend almost to surface it is not possible to match the measured gravity variation using a density contrast that is significantly smaller than the true contrast, but models can always be produced with too high a density contrast. The density contrast value was calibrated by matching the base depth of gravity models using different density contrast values to the acoustic basement depth from seismic and to the tops of magnetic model bodies assumed to represent magnetisations truncated at the basement unconformity. These tests support the initial density contrast estimate of 300 kg/m^3.

For convenience in constructing and manipulating the gravity model I decided to use grid traverses perpendicular to the trend of the gravity field rather than profiles of gravity stations. This option was feasible because the field variations of interest are well sampled by the 2.5 km station spaced survey and are reliably represented in the gravity grid derived from that data. I inverted the terrain-corrected Bouguer gravity data. The data already correct for small gravity variations due to terrain and allow use of a model with a horizontal top. I generated a set of 31 parallel traverses at a spacing of 6250 m and on those traverses defined a regional field that is slightly higher than the Bouguer gravity values beyond the basin edges. This regional field is high to the north through to low in the south, representing a broad field variation not necessarily related to the basin. This regional field variation could have been included as a wider and much deeper density contrast surface in the model but that would require additional work which would not have added value to the modelling objective. Once the regional gravity field is defined the task of the gravity model is to explain the ('residual') difference between the measured and regional fields. The difference is considered the anomalous field to be explained by the anomalous negative density contrast of the basin sediments against the basement of reference density. This approach conveniently avoids the need for a model body to represent the basement.

I constructed a starting inversion model using a polygonal-section horizontal prism with a strike length of 190 km to match the strike length of the basin and used this model to test the density contrast value. The horizontal top surface of the model is defined by only the two end vertices and the bottom surface is defined by vertices positioned beneath local gravity minima and maxima. After manual adjustment of this model quickly achieved an approximate match to the measured gravity data I reduced the strike length of the body to be the same as the data traverse spacing of 6250 m and duplicated it beneath each grid traverse to generate a continuous model of 31 adjacent strips, initially identical to the single body of the same cross-section and similar strike length. To invert this new composite body I first inverted the central strip of the model allowing only vertical adjustment of the bottom surface vertices to best fit the data on the central traverse immediately above it (all the model strips contributed to the forward field computations). Subsequently I similarly inverted the model strips to either side of the central strip to best fit only those traverses. These adjustments slightly reduced the data-fit previously achieved on the central traverse. However, because the density contrast is only shallow (a maximum depth of 3 to 4 km compared to a strip width of 6.25 km) gravity variation along each traverse can be matched with just a few iterations of individual or adjacent model strips or with one simultaneous inversion of all strips beneath the activated profiles. In this iterative fashion I worked out to both ends of the model, at which stage the combined fields of the complete set of model strips representing the basin matched the field on the complete set of traverses representing the anomaly.

The stepwise discontinuities between adjacent model strips occur halfway between the traverses where they are least significant to the measurements that are all computed on the central axes of the strips. Figure 2.21A shows an example model strip and the field computed from the complete basin model on the traverse above it. This model section clearly shows the two half-grabens with steep external basin margin faults and more gentle basement slopes to a central intra-basement high. Figure 2.21B shows the segmented model that reproduces the complete basin anomaly. The green-coloured segments in the south are controlled by the new higher-resolution data and the yellow segments to the north by the older, lower-resolution data. This model should not be envisaged as a final product but as an interim model best justified by currently available data and suitable for designing next-stage exploration of the basin. When any new data becomes available this model can be updated as required. Any additional information from closer-spaced gravity or airborne gravity gradient (AGG) data would mostly be significant in the narrow regions of abrupt gravity variation over the bounding faults.

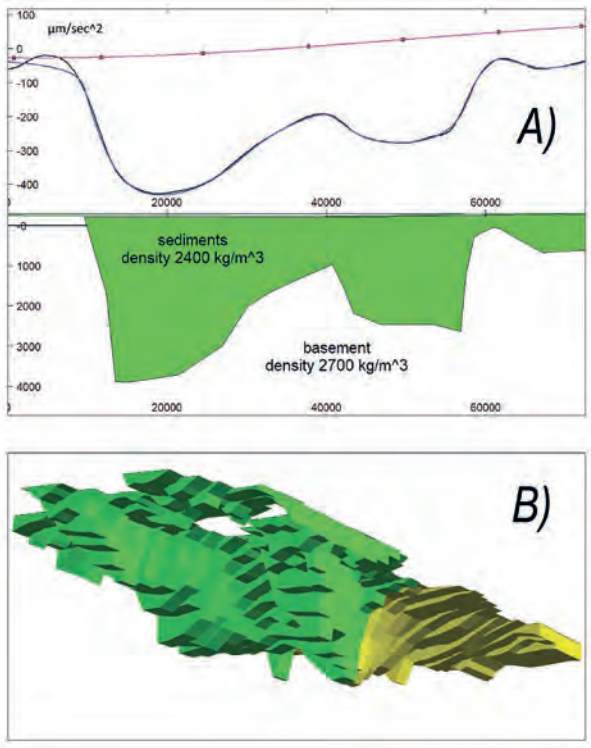

Fig. 2.21. A) example model section slice and B) perspective view of the multi-slice model. The green section is developed from the new high-resolution data and the yellow section from the older lower-resolution data.

2.7.2 Magnetic field modelling and inversion

The previous magnetic field coverage of the area was from surveys flown on east–west flightlines at 1,600 m spacing and ground clearances of between 60 and 100 m. The reduced to pole (RTP) field computed from this data is shown in Fig. 2.22A. Flightlines are not shown because at this scale they would obscure the image. Figure 2.22B shows an equivalent image from more recent magnetic field surveys with line spacings between 150 and 400 m and ground clearance of 60 to 80 m. The major features evident in the recent survey image of Fig. 2.22B are also evident in the older survey image of Fig. 2.22A. This is in part because many features are elongate perpendicular to the flightline direction and even in the wider line-spaced survey they have multiple flightline intersections.

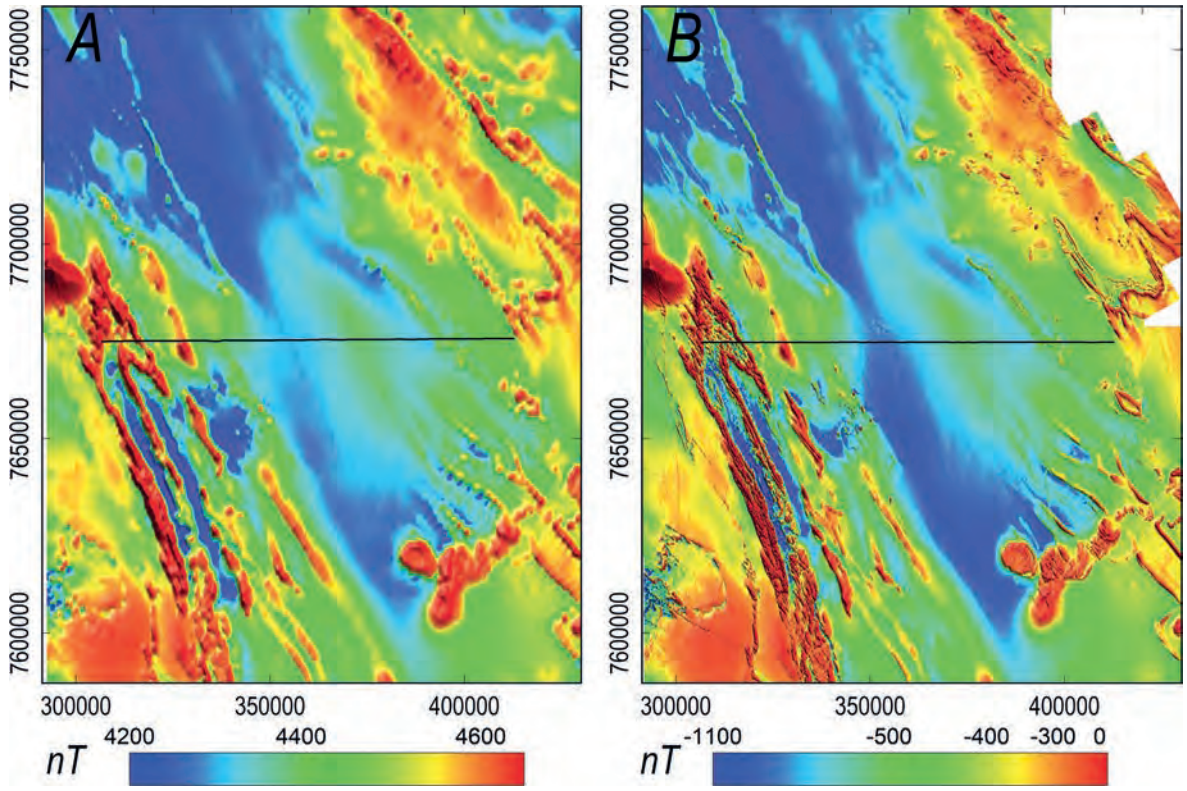

Fig. 2.22. TMI from A) previous 1,600 m line-spaced data and B) new 400 m line-spaced data.

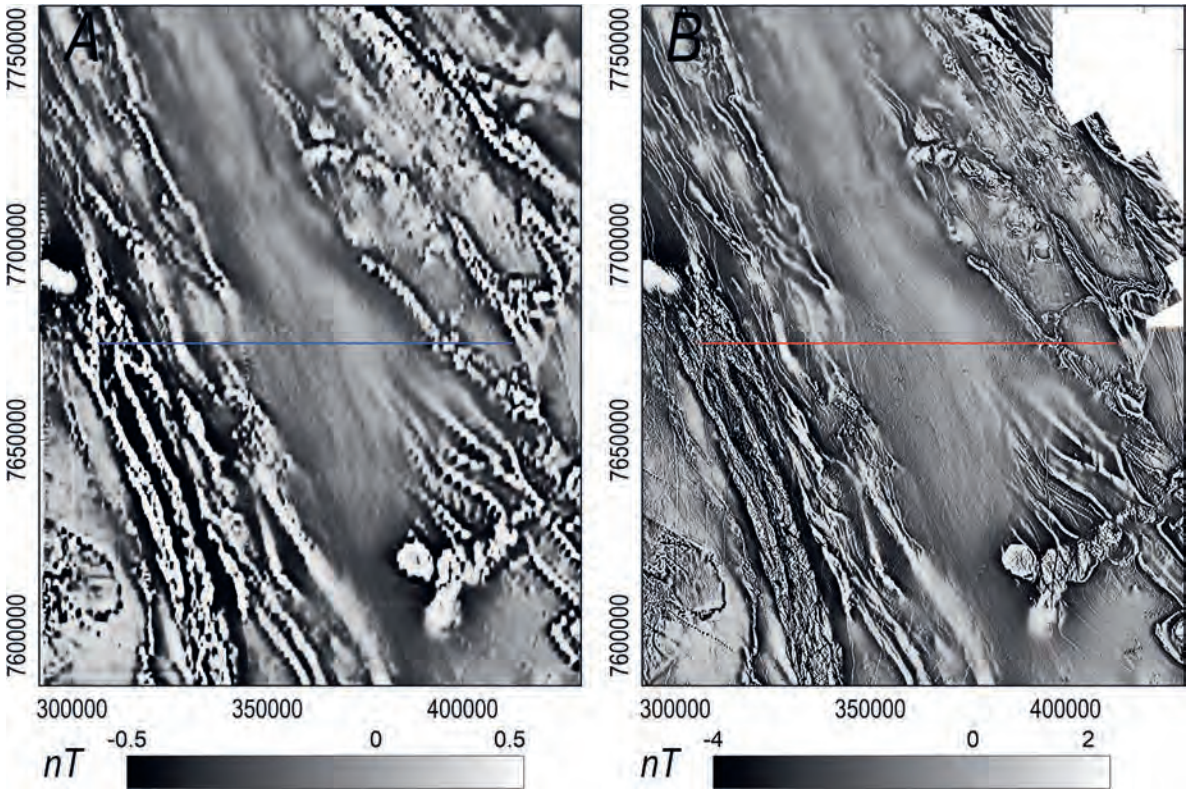

Fig. 2.23. The vertical derivative of TMI from A) previous 1,600 m line-spaced data and B) new 400 m line-spaced data.

However, all features are more sharply resolved by the closer line-spaced survey. Figure 2.23 shows corresponding vertical derivatives of the RTP. As for the gravity field, the gradient enhancement of the magnetic field benefits more from the closer line spacing than the field data do. I did not need to pre-condition this magnetic field data with an upward continuation before computing the vertical derivative. However, enhancement of the older, more widely spaced line data has significant artefacts in the form of 'bicycle-chain' or 'string-of-pearls' patterns where the minimum curvature griding used cannot interpolate sharp gradients from one profile intersection to the next. This is consistent with the case made by Reid (1980) that a closer line-spaced survey is required if gradients are to be derived from the measured field data. The gridding artefacts are not evident in the vertical derivative of the closer line-spaced survey data in Fig. 2.23B and in consequence geological inferences about the source magnetisations can be made more reliably from this data (see for instance Alavi 2013).

Figure 2.24 shows a comparison of two almost coincident flightlines from the two surveys. Differences between the flightlines are inconsistent, in part possibly because the individual lines have local vertical and horizontal departures. Improvements in magnetic field measurement and processing have been incremental but cumulative between the acquisition of these two surveys but more significantly there has been a major improvement in navigation and positioning, which went through a revolutionary change in the early to mid-1990s with the advent of GPS and differential GPS positioning that are critical to support the close line spacing of high-resolution aeromagnetic surveys. As with the gravity data, the differences between the two vintages of magnetic survey are due much more to the difference in data density than in data quality.

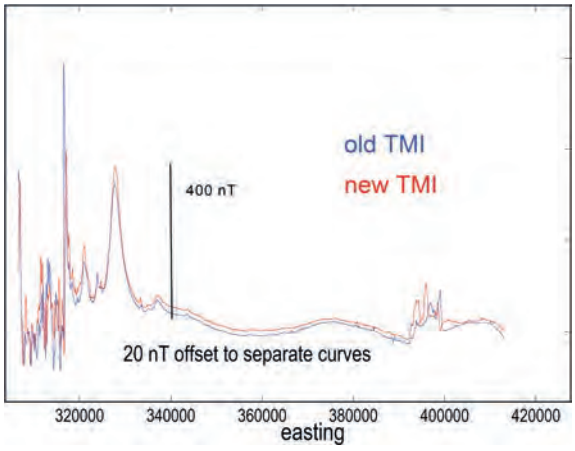

Fig. 2.24. Co-located profiles of previous and new survey TMI data.

Gravity and magnetic field characteristics are consistent with the same potential field theory, with reduced to pole (RTP) magnetic fields due to a transformed vertically directed magnetisation in a transformed vertical magnetic field equivalent to the vertical derivative of the gravity field (Blakely 1995). However, the vertical gradient of gravity images in Fig. 2.19 recognisable as enhancements of the gravity field images in Fig. 2.18 are very different to the RTP magnetic images in Fig. 2.22. This difference arises predominantly from differences in distribution of contrasts in the causative properties of density and magnetisation. As discussed above, the gravity field variation is primarily determined by the bulk difference in property of the complete basin against the complete basement and this determines the approach to the gravity inversion. That approach is not feasible and would not be productive for inversion of the magnetic field data. Much of the basement has magnetisation similarly low or not much greater to the magnetisation of the basin sediments, and across the basement unconformity surface there are only small areas of useful magnetisation contrast. Instead, the magnetic field variation is dominated by fields of strong magnetisations of minor, shallow parts of the basement. The consequence of this is that a combined inversion of gravity and magnetic fields at this scale is unlikely to be productive. Instead, the undoubted benefits to be gained from investigating the two fields due to different properties is best exploited by ensuring compatibility between the output models of the two independent inversions, or else by introducing the results of one inversion as constraints in the other. The magnetic field expression of the basin is most obvious as the absence of sharp anomalies due to local, strong magnetisations present in the surrounding areas of shallow basement. This absence of anomalies is not readily exploited in an inversion. There is a weak magnetic field expression of the two basin deeps evident in the gravity images and resolved in the gravity inversion. In the magnetic field image these appear as subtle magnetic lows separated by a weak magnetic high over the central basement and gravity high. This demonstrates a weak contrast in magnetisation between the bulk basement and the basin sediments, but the magnetic field variation (evident in the images because of histogram equalisation) is of such low amplitude that a combined gravity and magnetic

inversion would be unlikely to be of advantage. Instead, I inverted the magnetic field data just as in the previous magnetic field studies using the sweet-spot approach of focussing individual inversions on small individual packets of information in the magnetic field data.

Figure 2.25 shows an example sweet-spot magnetic field inversion of two source bodies. Their source depths can be estimated in the following steps:

1) draw a grid traverse through the anomalies
2) extrapolate magnetic field and ground surface grid data onto the traverse and add the nominal flying height of 60 m to the ground elevation to represent the sensor height
3) choose an appropriate source model (for these bodies which I assume to be truncated at an unconformity I selected tabular prisms with horizontal top and bottom surfaces)
4) place the bodies under each anomaly and in map view adjust their strike length and azimuth to approximately match the anomalies
5) assign a background or regional field to which the body fields will be added to match the anomalies
6) adjust the depth and magnetic susceptibility of the bodies to produce an approximate starting model for the inversion
7) select appropriate free parameters for the inversion – in this case depth, depth extent, width, dip and magnetic susceptibility of each body. Note that their azimuth and strike extent should not be changed as there is almost no sensitivity to these parameters on the single data traverse
8) if the inversion converges acceptably it provides estimates of each body parameter.

In areas of the shallowest sources I modified the above procedure to use measured flightline data and avoid concerns of the magnetic field gradients being modified in the process of gridding and subsequent interpolation. This sweet-spot method utilises only the most appropriate data for source depth estimation. The location where depth estimates are derived and the spatial density of the estimates is controlled by the magnetic field data. In some areas there are many suitable anomalies and a selection of those anomalies was made for analysis, in other areas the analysis had to be applied to

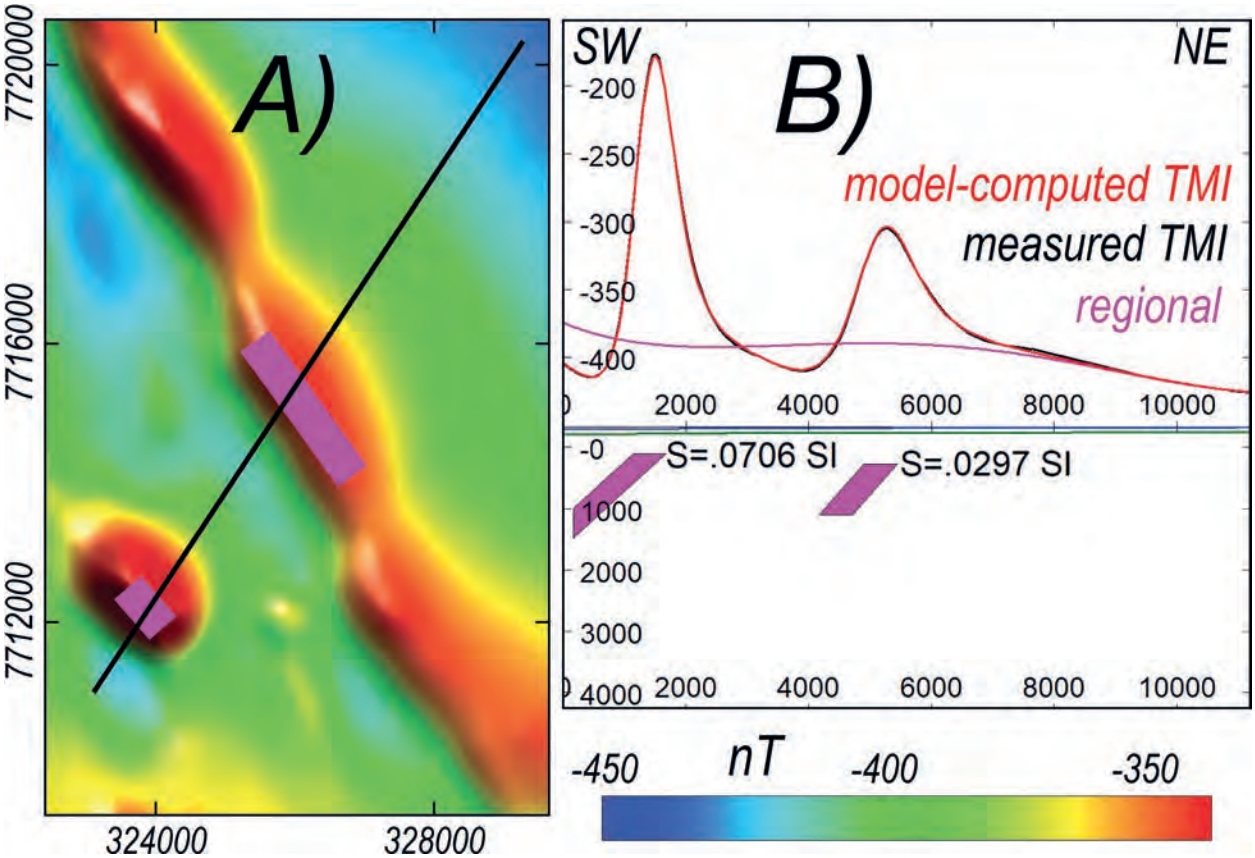

Fig. 2.25. Magnetic depth traverse: Top) cross-section view and Bottom) plan of the traverse over an image of TMI.

less suitable anomalies and in some places there were no suitable anomalies from which meaningful depth estimates could be derived. There are many suitable anomalies over shallow basement where small magnetised bodies can be detected. Where basement is more deeply buried there are fewer suitable anomalies.

Full three-dimensional inversion of the magnetic bodies can give a more reliable representation of the magnetisation but provided the strike and azimuth of the model bodies are appropriate to match the anomalies, a superior estimate of depth to the top of magnetisation is derived by closely fitting the field gradients on well-selected individual profiles. The depth estimates are to the top of magnetisation, but these magnetisations are not stratigraphically attributed. To investigate the Palaeozoic Waukarlycarly Graben all magnetisations truncated at the base of the basin fill can be classified as Proterozoic basement, but for mineral exploration within the Palaeozoic basement it is of advantage to discriminate between magnetisations sourced in separate units.

The spot depth estimates are the most reliable depth information recovered from the magnetic field analysis. In many cases a depth surface is required (in this case the elevation of Proterozoic basement) and these surfaces must be interpolated between the relevant depth points. Geological surfaces can be complex and include abrupt discontinuities so any interpolation is necessarily speculative and interpretive. Any interpreted depth surface should always be accompanied with the depth points from which it has been constructed.

Figure 2.26A shows the ensemble of magnetic source depth models. Normally a depth surface would be constructed by gridding of the top surface depth points or by drawing the surface in a three-dimensional GIS environment (including any boreholes or depth-converted seismic sections) but in this case bodies were imported to provide guidance in the gravity modelling and inversion where the base of the basin infill gravity model is expected to coincide with tops of the intra-basement magnetic models. This correspondence was very strong as shown

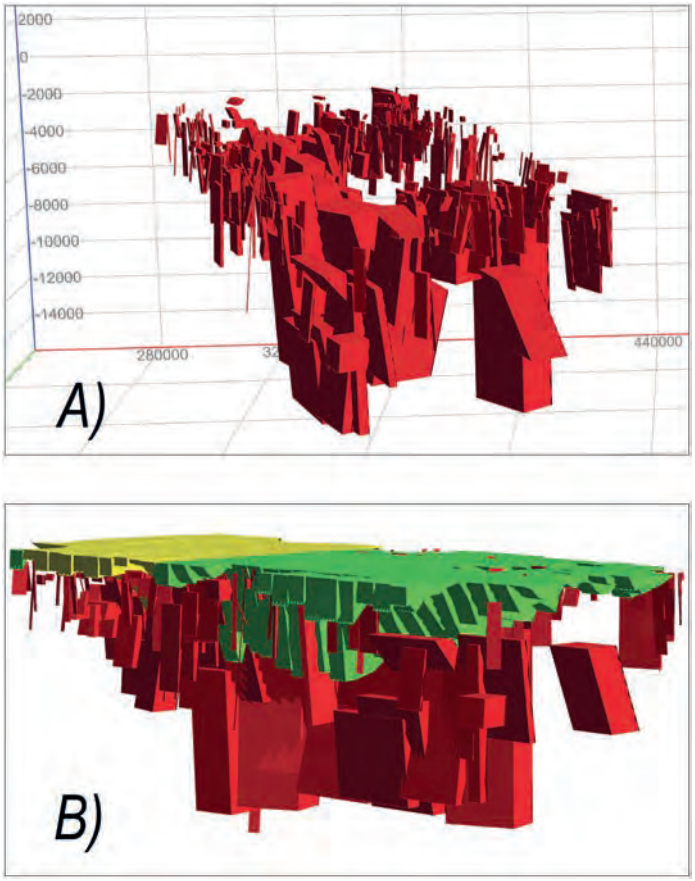

Fig. 2.26. A) Ensemble of magnetic depth models and B) combination of the gravity basin model (yellow and green) and intra-basement magnetic models (red).

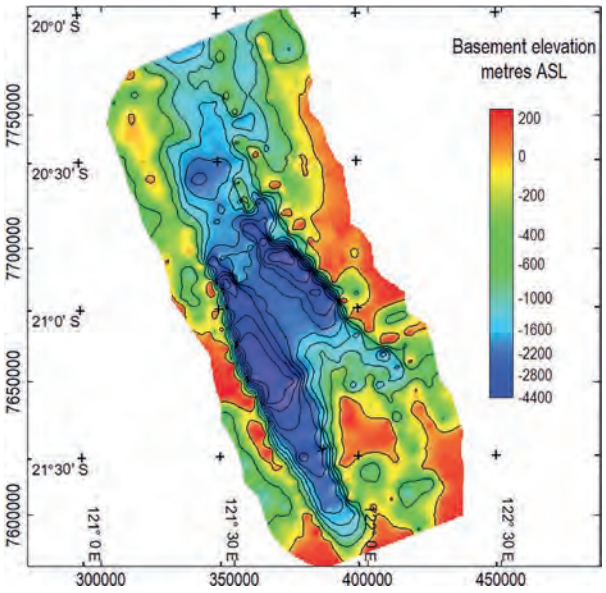

Fig. 2.27. Top of basement elevation map.

by the view of the combined gravity and magnetic inversion models in Fig. 2.26B. The final Palaeozoic basement surface imaged in Fig. 2.27 was derived from gridding of the vertices defining the base of the gravity model but a near-identical surface would be derived from generating a surface through the tops of the magnetic models.

The major conclusion I draw from the Waukarlycarly case study is the need for careful and detailed measurement of the fields and understanding of the relationships between geology, physical properties, and the gravity and magnetic fields. Information can then be efficiently recovered with focus on suitable features in the fields.

2.8 THE INFLUENCE OF GRIDDING ON INVERSION

Gridding is often considered a passive repositioning of data from measurement points to nodes of a regular mesh. However, grid data is a new data type significantly different to the primary data and this has significant consequences. Grid data are convenient to use but unquestioned acceptance of grids as valid representation of a gravity or magnetic field is a common and serious problem in gravity and magnetic studies. The influence of gridding is least significant where measurements have been acquired on a regular mesh which requires little or no adjustment of the primary data values to minimally displaced grid cell positions. Gridding is most significant where data have variable spacing or (as for aeromagnetic data) with different spacings in along-line and cross-line directions. Over the last few decades many magnetic field grids have been generated with algorithms based on the minimum curvature method of Briggs (1974) which assigns grid characteristics broadly consistent with expected potential field variations. A grid cell size of one-quarter or one-fifth of the line spacing is commonly chosen as a compromise between retaining as much detail of the line data as possible and restricting distortion in interpolation between lines. One of the most distinctive gridding artefacts of profile data is known as a 'string-of-pearls' or 'bicycle-chain' pattern where a linear sharp gradient in the field breaks down to a series of individual features at each profile intersection. This artefact is visible in the south-eastern segment of the Waukarlycarly wide line-spaced magnetic field data in Fig. 2.22A and because the vertical gradient has sharper curvature than the field itself the artefact is more strongly emphasised in the corresponding vertical gradient image in Fig. 2.23A. In this study I investigate limitations in inversion of grid data with these artefacts to recover estimates of depth to the top of magnetisation. The artefacts represent only a small proportion of more widespread and cryptic problems with grid data. Recently new and more sophisticated methods of anisotropic gridding have been published (Naprstek and Smith 2019; Davis 2022). However, no gridding methodology completely compensates for insufficiencies in distribution of the primary data.

Figure 2.28 shows a section of the south-east-north-west trending swathe of prominent Gairdner Dyke magnetic field anomalies near Mount Vivian in South Australia (Foss *et al*. 2019; Pawley *et al*. 2021). The survey was flown on north–south flightlines at a spacing of 200 m and nominal terrain clearance of 60 m as part of the Gawler Craton Airborne Survey (GCAS) project (Katona *et al*. 2021) and the grid was well produced within the capabilities of the minimum-curvature method used. The dyke anomalies have subtle expression of 'string-of-pearls' or 'bicycle-chain' artefacts at each profile intersection, mostly evident in sun-shading of the image. Figure 2.29 shows a contour map of the single anomaly inset in Fig. 2.28. For this anomaly tight contour closures mark each profile intersection with the anomaly. The contour interval is 10 nT and the amplitudes of the artefacts are up to 35 nT on an anomaly of peak to trough amplitude 240 nT. Figure 2.30 shows profile modelling of a north–south flightline. The anomaly was inverted with an assumption that magnetisation is due only to induced magnetisation. An identical inversion was

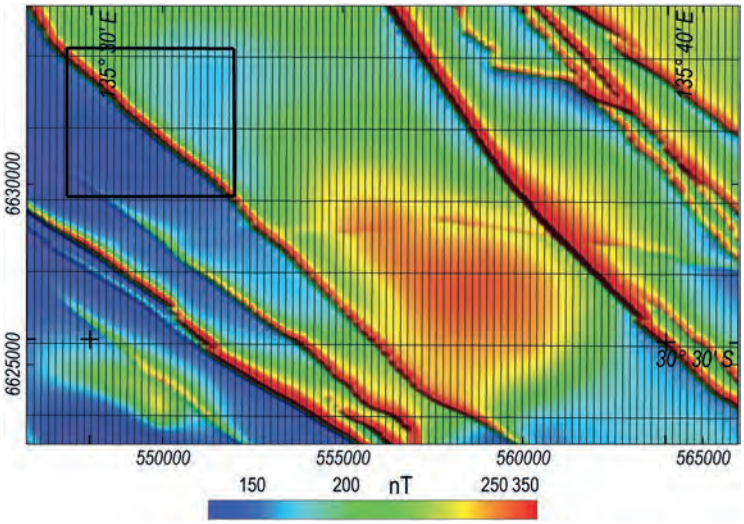

Fig. 2.28. TMI image of a section of the Gairdner Dyke Swarm, South Australia with inset of the single-dyke study area.

performed of an east–west tie-line that intersects the anomaly at the same location (see Fig. 2.29). Inversion of these independent lines of data produces two consistent models with key statistics listed in Table 2.1. The difference in depth to their tops is only 5 m in an average depth below sensor of 108 m. For this study the mean of these estimates is accepted as the best available depth for the top of the dyke. There is a difference of less than 4° between the apparent dip estimates of the dyke models derived on the two orthogonal lines.

Figure 2.31 shows a contour plot from an alternative gridding of the data using the anisotropic method developed by Naprstek and Smith (2019) and implemented in the Oasis Montaj software package (grid provided by

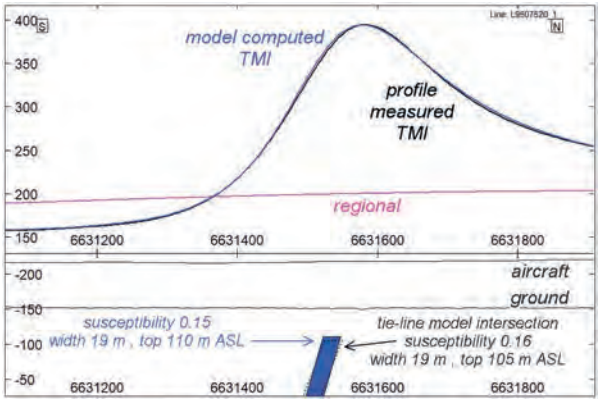

Fig. 2.30. A model section on north–south flightline L9507520 (for location see Fig. 2.29).

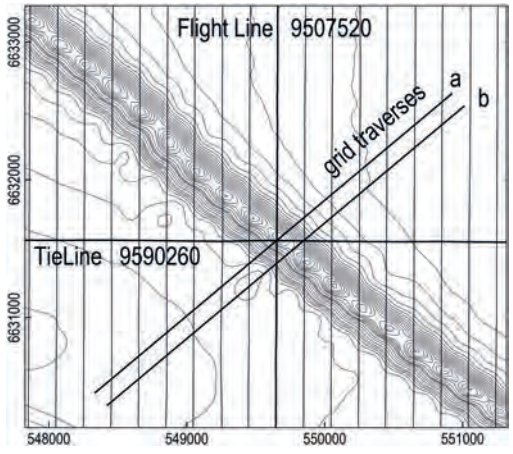

Fig. 2.29. Segment of a Gairdner dyke magnetic anomaly defined by a minimum-curvature TMI grid. The contour interval is 10 nT. The 'string-of-pearls' artefacts have amplitudes of c. 35nT and the anomaly amplitude is c. 240 nT.

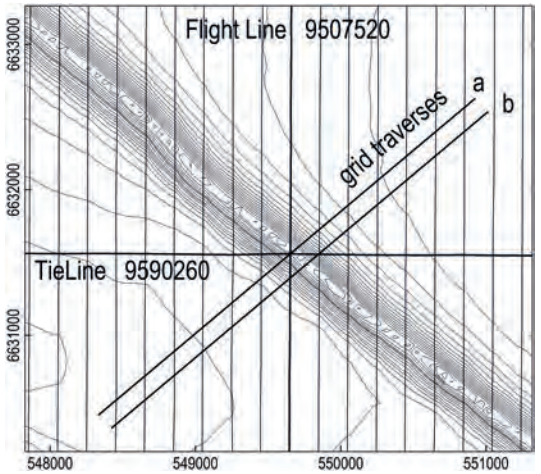

Fig. 2.31. Flightlines and grid traverses over anisotropic gridded TMI contour map. Contour interval 10 nT and anomaly amplitude c. 240 nT.

Table 2.1. Dyke inversion model statistics.

Grid	Line	Susc SI	Elev m ASL	Width m	Dip	Difference in depth below sensor	Difference in depth below surface
–	9507520	0.145	–110	19	75°		
–	9590260	0.157	–105	19	78°		
Min curv	9507520	0.145	–111	20	75°	3% (shallower)	7%
Min curv	west 100	0.0112	–154	227	81°	42% (shallower)	100%+
Min curv	a	0.016	–130	180	75°	20% (shallower)	51%
Min curv	b	0.013	–133	197	83°	23% (shallower)	58%
Anisotropic	9507520	0.137	–108	22	72°	0	1%
Anisotropic	west 100	0.131	–113	23	73°	5% (deeper)	12%
Anisotropic	a	0.146	–102	21	74°	5% (deeper)	14%
Anisotropic	b	0.137	–107	22	75°	1% (deeper)	2%

Cericia Martinez). The individual contour closures at profile intersections prominent in the minimum curvature gridding of Fig. 2.29 are removed and it is not feasible to locate line intersections from the gridded data. To investigate the consequence of inverting grid data I interpolated data channels from both the minimum curvature and anisotropic grids onto flightline L9507520 and inverted those channels. The data are modified not just in the process of creating the grids but also in the interpolation used to resample them onto the profile. The minimum curvature grid cell size is 40 m, the anisotropic gridding cell size is 50 m, and the average along line sample spacing is 3.5 m. Single profile inversions of both grid-interpolated datasets provide acceptable models, with depths consistent with the flightline model depths to within 5%. There is a slight northward shift of the interpolated anisotropic grid data results in a corresponding 25 m northward shift of the inversion model (one-half of the grid cell width).

Depth below sensor is an appropriate statistic to evaluate sensitivity of depth estimation but for geological exploration programs a more relevant measure is depth below the ground surface. The relationship between the percentage errors on these two depths depends on the ratio of depth to magnetisation below the ground and flying height above it, with proportional errors and uncertainties rising steeply for shallow magnetisations.

Inversions of the L9507520 flightline grid interpolations only test the consequences of inverting interpolated grid data in immediate proximity to the measurements. I also inverted data onto a grid traverse 100 m to the west, halfway to the adjacent flightline and intersecting the grid anomaly between the pearls of the minimum curvature gridding. Continuity of the anomaly on multiple flightlines indicates that interpolations along traverses between the flightlines should be the same as interpolations of traverses coincident with the flightlines. However, interpolation from the minimum curvature grid onto the intermediate traverse is quite different to the primary profile data on the flanking flightlines. The consequence of inverting the minimum curvature grid traverse away from the flightline is a significant increase in apparent thickness, decrease in apparent susceptibility by an order of magnitude and a decrease in depth to top of over 40% in depth below sensor and 100%+ in depth below the ground surface (see Table 2.1). This depth estimate would be useless and even misleading in an exploration program. In marked contrast, interpolation of the anisotropic grid on this traverse produces an anomaly similar to the directly measured profiles on the adjacent anomalies and its inversion recovers a model very similar to the profile data inversions with increases in depth of only 5% and 12% below sensor and below ground respectively.

A major advantage of using grid data for inversion is the freedom in position and orientation of traverses, which for elongate anomalies such as this Gairdner dyke anomaly would generally be selected perpendicular to the feature. Figure 2.32 shows two grid traverses perpendicular to the dyke (traverses ‘a’ and ‘b’ in Fig. 2.29); the first passing through a dyke and flightline intersection (through a minimum curvature gridding pearl) and the second midway between two adjacent pearls. These traverses do not have primary profile data to compare with the grid interpolations but we can confidently emulate

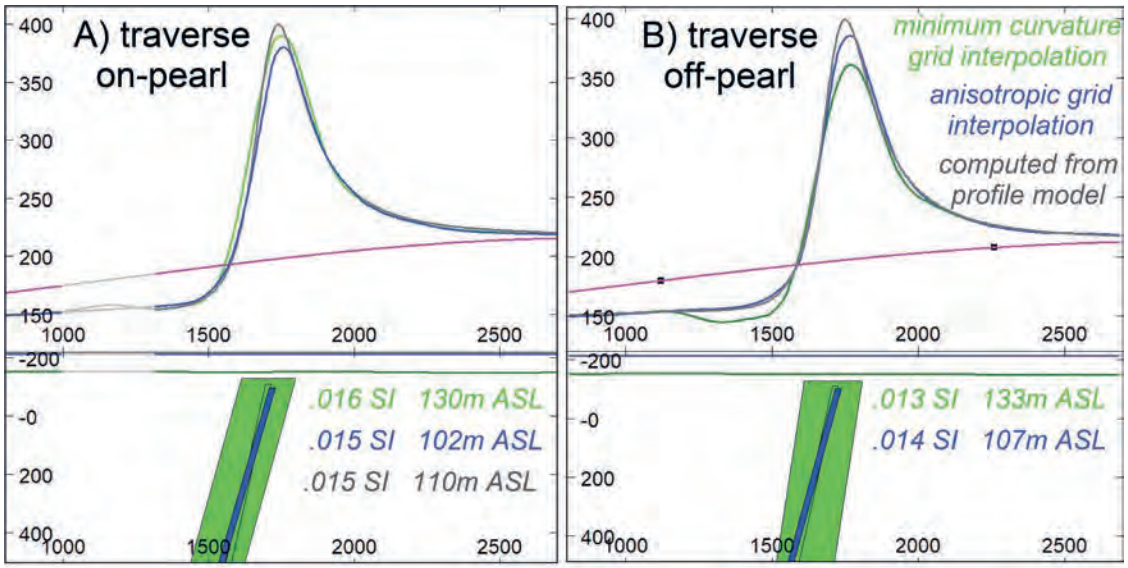

Fig. 2.32. Line 9507520 minimum curvature (mc) and anisotropic (an) grid interpolations and inversion model bodies.

that data using the already derived inversion model which closely matches the primary flightline data. On the interpolated curves along both traverses plotted in Fig. 2.32 the broader curvature of the minimum curvature grid data is obvious. The amplitude of the minimum curvature interpolation through the pearl (grid traverse 'a') is higher than on the grid traverse between the pearls (grid traverse 'b') but the erroneous curvature is similar on both traverses. Because of the erroneous curvature of these data the dyke models derived from its inversion are also in error. The models are substantially wider and with lower apparent susceptibilities than the profile data inversion models and are shallower by over 20% of depth below sensor and over 50% of depth below ground (see Table 2.1).

The data interpolated onto the traverses from the anisotropic grids have curvature more consistent with the field forward computed along the traverses from the profile data inversion model. Inversions of the anisotropic grid data also produces models more consistent with the profile data inversion model (see Table 2.1). The models from inversions of both lines have widths and susceptibilities similar to the profile data inversion models and increases in depth of 5% below sensor and just over 10% below ground. These imperfections in inverting grid data increase for shallower magnetisations with sharper gradients and for surveys of wider line spacings (inversion model imperfections are also greater for anomalies over bodies with short strike length that give rise to sharp field variations in all horizontal directions).

This Gairdner Dolerite dyke study clearly shows that for depth to top of magnetisation one-half of the line spacing and with 'string of pearls' artefacts weakly evident, minimum curvature gridded data misrepresents the magnetic field to cause over 20% difference in estimates of depth to the top of magnetisation compared to estimates made directly from the profile data. Anisotropic gridding reduced those differences to 5%. Further systematic studies are required to map these inadequacies in grid data as a function of line spacing, depth to magnetisation and magnetisation body geometry. For a single survey dataset there are only minor overheads in using profile data for inversion and this should be the preferred option. If depths to top of magnetisation are less than one-half of the line spacing, use of grid data becomes less acceptable and gives increasingly misleading results. Unfortunately, this problem is unlikely to be detected if only grid data are inverted because inversions still match that data very closely. Use of micro-levelled grids is a further concern because micro-levelling also distorts representation of the magnetic field with little evidence from which that distortion can be recognised or corrected. Unfortunately, some clients of aeromagnetic surveys focus only on the grid deliverables from the contractor and the line data may be unavailable for depth estimation and inversion. The grids may also become separated from the processing report and metadata which records the operations and settings applied to generate them. It is safer to invert profile data unless there is a pressing reason otherwise.

2.9 THE USE OF VERTICAL GRADIENT ENHANCEMENTS IN INVERSION

The previous study of the Gairdner dykes dealt with issues related to horizontal gradients of the magnetic field for a case that they vary in a single horizontal direction. Cross-line horizontal gradients can be measured with advantage in aeromagnetic surveys with wing-tip mounted sensors and along-line horizontal gradients can be derived from the closely spaced sequential measurements. The vertical gradient of TMI has been measured on aeromagnetic surveys using vertically displaced sensors on the tail fin of the aircraft (Hood and Teskey 1989) but this application faces challenges of low signal to noise ratios. Fortunately, the vertical and total horizontal gradients form a Hilbert pair (Blakely 1995) and the vertical gradient can be derived by a two-dimensional FFT of horizontal gradients estimated from closely spaced TMI measurements in the horizontal plane. The two-dimensional FFT filter to derive a map of the vertical gradient of TMI from a horizontal survey of TMI data requires construction of grids with the corresponding limitations discussed in the previous section, and with the increased resolution requirements of gradient data as discussed by Reid (1980). Gradient measurement of the three orthogonal field components to give the second-rank gradient tensor (Schmidt *et al*. 2004; Chwala *et al.* 2012) has considerable advantage in detailing small and shallow magnetisations but the increased cost of acquisition of these data has to present restricted its use.

Figure 2.33A shows an image of a minimum-curvature TMI grid of the Elkedra Area in the south-east Northern Territory derived from a survey flown on north–south flightlines at 400 m line spacing and a nominal 60 m terrain clearance. The TMI variation is dominated by a series of curved, elongate anomalies of 100 to 200 nT amplitude. The near-surface geology is shallow marine to fluvial sediments and interbedded felsic and mafic volcanics of the Proterozoic Davenport Province Hatches Creek Group (Blake and Horsfall 1986). The prominent anomaly imaged in Fig. 2.33A is sourced in a recessive volcanic unit near the base of the Alinjabon Sandstone in the Errolola Syncline (Fig. 2.33B). Figure 2.34A shows the minimum curvature

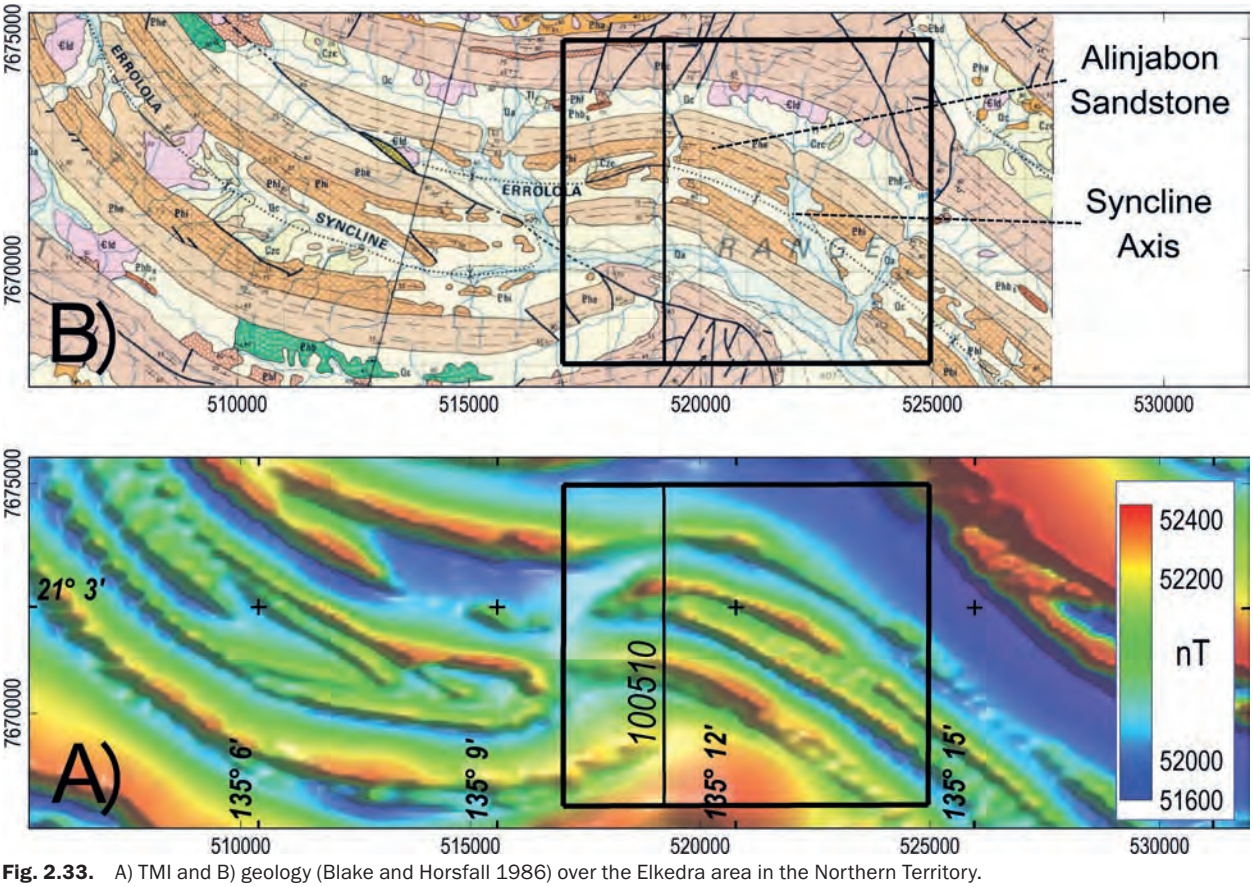

Fig. 2.33. A) TMI and B) geology (Blake and Horsfall 1986) over the Elkedra area in the Northern Territory.

grid in the inset area of Fig. 2.33. The bicycle-chain or string-of-pearls artefacts in this image are much more pronounced than those over the Gairdner dykes in the previous section. The magnetisations in the two areas are of similar depth, width and elongation but the line spacing in the Elkedra area is twice that of the Gairdner area. Re-gridding of the data with the anisotropic method of Davis (2022) created the grid imaged in Fig. 2.34B (grid supplied by Aaron Davis) which significantly reduces these artefacts and offers identical advantages for inversion as established in the previous study by the anisotropic gridding of Naprstek and Smith (2019). Gradient filters preferentially enhance the shortest wavelength features in data, which in the case of the minimum-curvature grid are gridding artefacts. The advantage of anisotropic gridding shown by comparison of the TMI grids in Fig. 2.34 is amplified in mapping the vertical derivative as shown in Fig. 2.35. Despite this significant improvement we will use the line data in investigation of these shallow magnetisations,

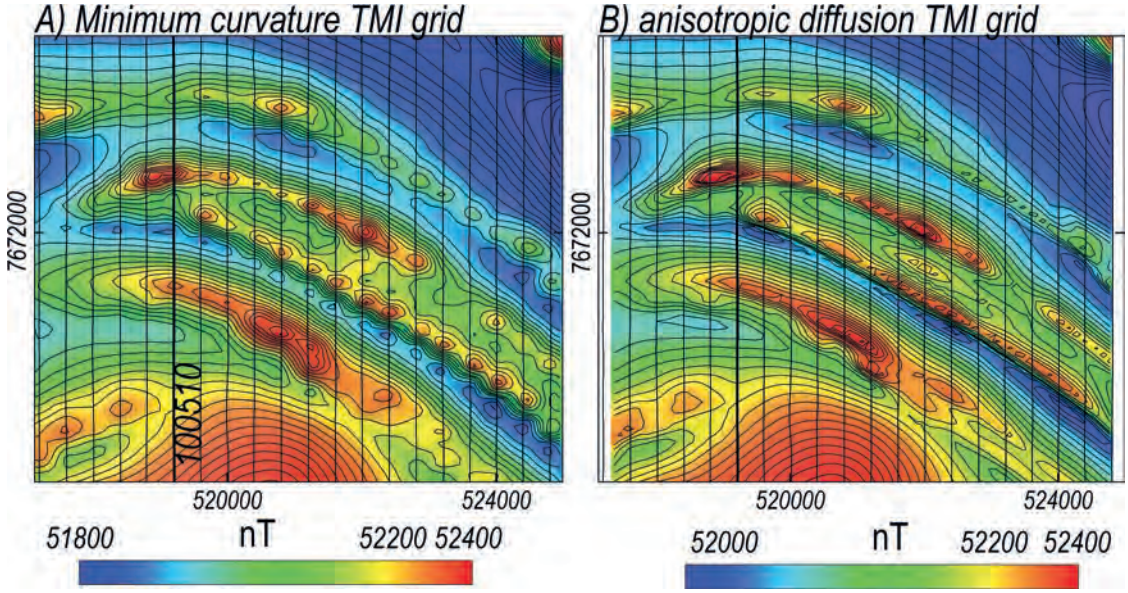

Fig. 2.34. Vertical derivative of TMI from A) minimum curvature gridding and B) anisotropic gridding (Davis 2022) for the inset area in Fig. 2.33.

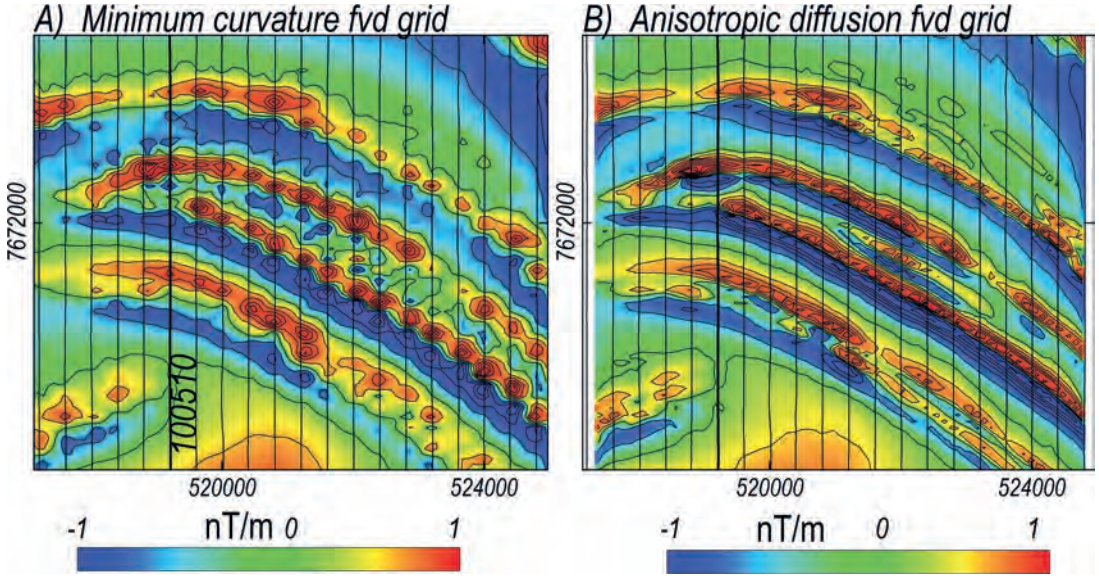

Fig. 2.35. Vertical derivative of TMI from A) minimum curvature gridding and B) anisotropic gridding (Davis 2022) for the inset area in Fig. 2.33.

particularly in consideration of applying gradient enhancements.

Figure 2.36 shows a model section along the north–south flightline 100510 located in Figs 2.33 to 2.35. The bottom section shows model bodies semi-automatically generated by the ModelVision implementation of AutoMag, a magnetic source depth estimator based on the method of Naudy (1971) and further developed by Shi (1991) and Shi and Boyd (1993) to analyse field gradients. The Naudy method nominates a target source body – in this case a dyke of specified width and top depth ('dyke' is used as a geometric term for a thin sheet). The TMI expression of the target body in a nominated window width is split into symmetric and asymmetric parts, moved along the measured profile and cross-correlated with a similar splitting of the measured field (in this case the splitting is applied to vertical derivative filters of those fields). Where the correlation coefficient triggers a solution a more advanced analysis is performed, followed by a simple table-lookup inversion. In this method the solutions contain all the information required to convert them to model bodies that can be tested against the primary data by forward modelling. To match the measured and model-computed TMI shown in the centre track of Fig. 2.36 clearly requires addition of a long wavelength background field gradient. The vertical gradient filters of measured and computed TMI shown in the top track of Fig. 2.36 match much more closely than the equivalent field curves in the TMI track below because the gradients are only weakly sensitive to the regional field and because analysis was tuned to the gradient filter. The vertical derivative of TMI has the advantage that it is more sensitive to the shallowest magnetisation, that it has only low sensitivity to the regional gradient, and that the anomalies are compressed which reduces overlap of adjacent body fields. In using the profile data to retain the advantage of its close sample spacing and avoid griding artefacts we do not have access to the cross-line gradients. The initial Automag analysis is performed on a two-dimensional assumption that source magnetisations are perpendicular to the line and extend large distances to either side, in which case there is no horizontal cross-line gradient. With only the along-line component of the horizontal gradient available the vertical gradient filter may not provide a valid estimate of the true vertical gradient of

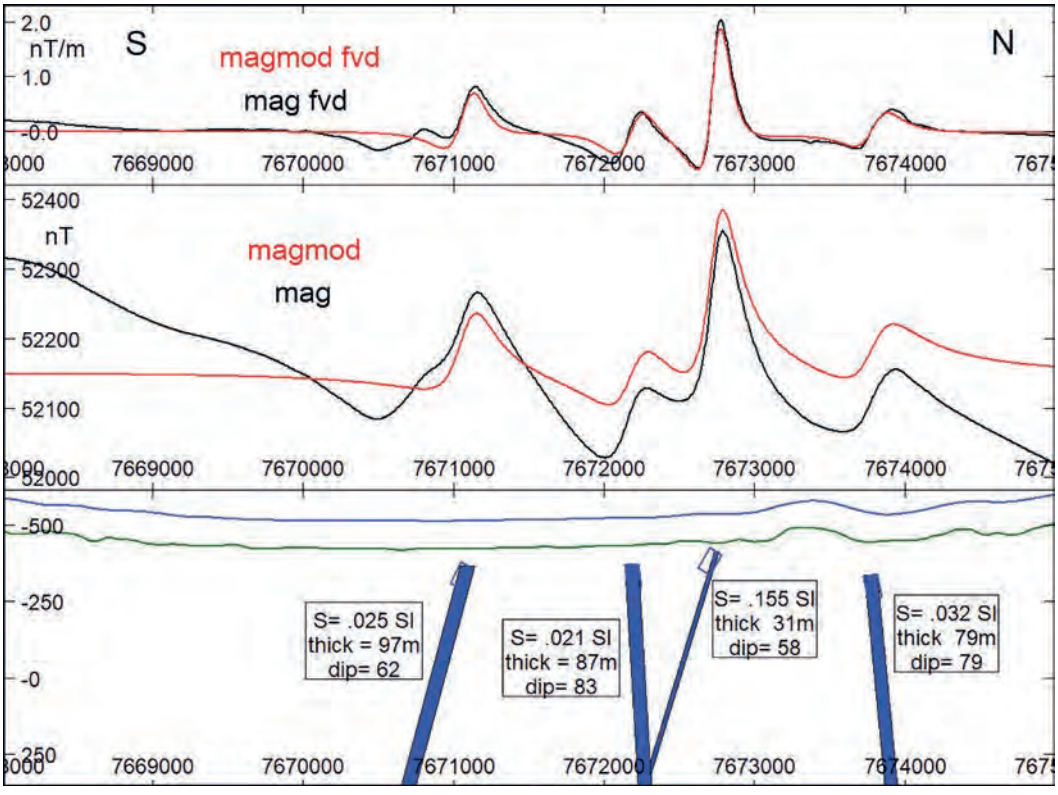

Fig. 2.36. South to North flightline 100510 with (bottom) source bodies generated from Automag solutions, (middle) measured and model-computed TMI, and (top) linear filter vertical derivatives of measured and model-computed TMI.

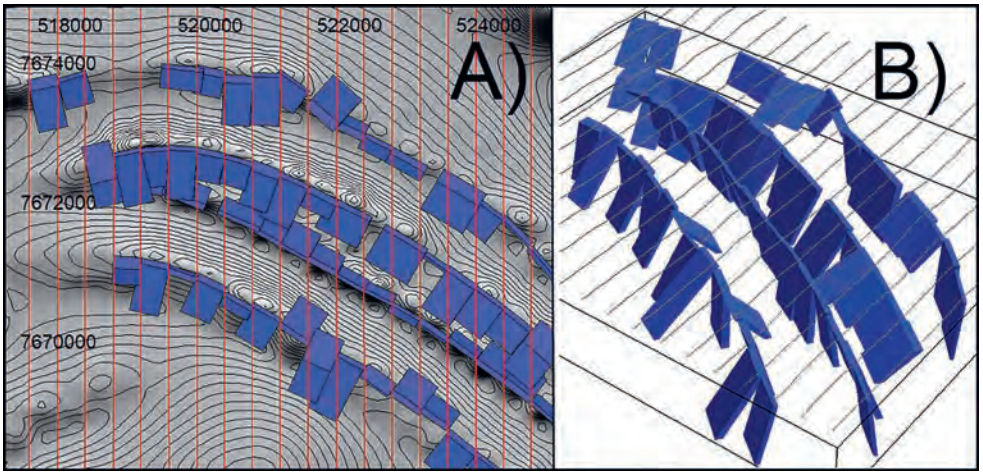

Fig. 2.37. A) plan view of strike-adjusted Automag-derived source models over an image of TMI, and B) perspective view of the source models.

the field. However, comparison between the vertical gradient filter of the data and the identical vertical gradient filter of the model-computed field remains valid. Even if the filter is not the true vertical gradient it provides similar advantages.

I finetuned the first phase analysis on the selected flightline to optimise solutions from the anomalies of interest while reducing inappropriate or unwanted solutions, and then generated solutions in batch mode on all the lines. I then converted those solutions with a second phase analysis to source model bodies as shown in map view in Fig. 2.37A. This operation requires rotation of the solutions to their true orientation with associated adjustment of their parameter values. Rotation can be performed using the local field trend interpolated from a suitable grid (ideally based on anisotropic gridding of Naprstek and Smith 2019 or Davis 2022). In this case, I selected sequential solutions along individual anomalies which the analysis reorients to align the bodies 'head to tail'. As this realignment is performed the parameter values are automatically adjusted for rotation to their new strike direction. Figure 2.38B shows a perspective view of the rotated solutions which clearly represent the Errolola syncline and provide an excellent starting model for inversion. This model with a body at each profile and anomaly intersection was more complex than required and I thinned it to fewer, longer bodies before proceeding to a user-guided inversion. Figure 2.42 shows the post-inversion flightline model of Fig. 2.40. Just as with Automag, I tuned inversion to match the line-based vertical derivative filter. Vertical gradient inversion should not modify the regional field or the depth extent of bodies because of lack of sensitivity to those parameters, but if required those values can be adjusted with interspaced TMI inversions. For instance, I adjusted the centre body depth extents to restrict 'scissoring' (see Fig. 2.40) to which there is little model sensitivity even in the TMI inversions. Having produced a good general fit to the data, any subsequent improvement of individual bodies is best achieved by inverting only that body or a combination of immediately adjacent bodies to best fit local selections of the data. Any nearby bodies with overlapping fields must be included in the forward modelling calls of inversion even if those bodies are not inverted themselves.

The Elkedra study illustrates the considerable power of tuning inversions using gradient data of the primary, closely spaced flightline measurements with suitable

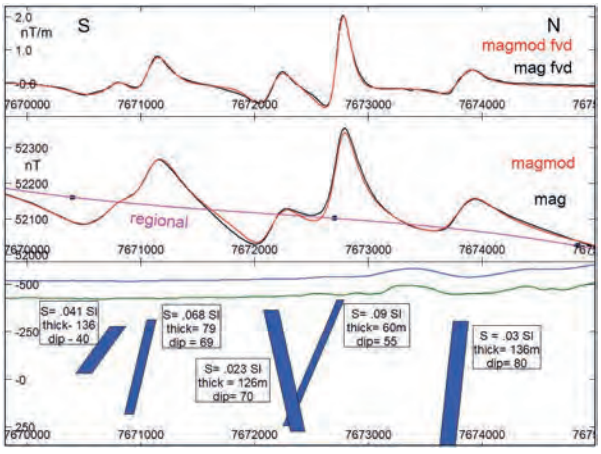

Fig. 2.38. South to North flightline 100510 with (bottom) source bodies from vertical derivative inversion, (middle) measured, regional and model-computed TMI, (top) linear filter vertical derivatives of measured and model-computed TMI.

strategies to compensate for loss of cross-line horizontal gradients.

2.10 USE OF GRADIENT ENHANCEMENTS TO SEPARATE FIELDS THAT CAN BE MEANINGFULLY INVERTED FROM THOSE THAT CANNOT

Many consumers and some authors of inversion models assume or accept that inversion software has sophistication buried within it to produce definitive models. Unfortunately, this is not true. Inversions produce models which should be (at least mathematically) possible explanations of the measured field. However, without input of considerable independent information inversion cannot resolve fundamental non-uniqueness and models are not definitive because they have been developed by an inversion. In the previous Elkedra case study I illustrated how gradient data can be used to improve recovery of shallow magnetisation models. In this case study I will show that for a model to be meaningfully derived by inversion (still not for it to be uniquely defined) it must primarily focus on explaining data features that dominate curvature of the measured magnetic field.

Figure 2.39 shows a TMI image of the Cobham Lake area in north-west New South Wales. The survey was flown as part of a regional geological mapping program on east–west flightlines at 250 m spacing and a nominal 60 m terrain clearance. The area has extensive regolith cover, sparse basement outcrop and few boreholes. The geological map in Fig. 2.40 (Hegarty 2017) was developed

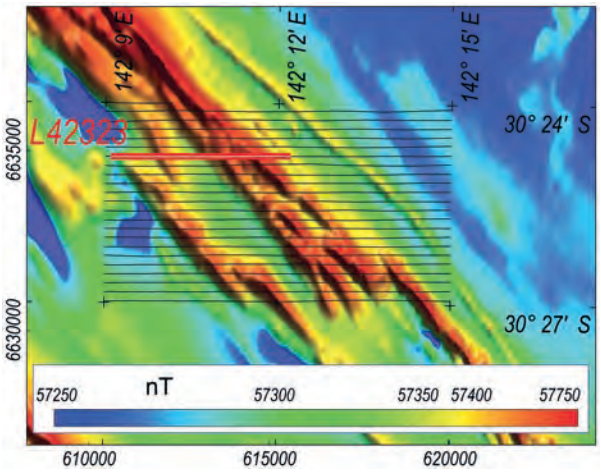

Fig. 2.39. TMI image and 250 m spaced east–west flightlines near Cobham Lake, New South Wales.

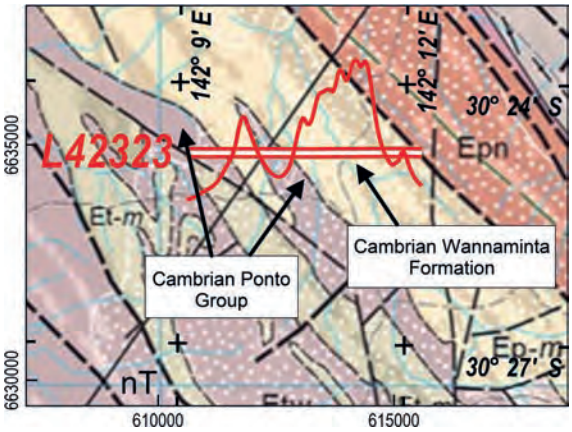

Fig. 2.40. Location of the sections in Figs 2.41 and 2.42 over the Cobham Lake geological map (Hegarty 2017).

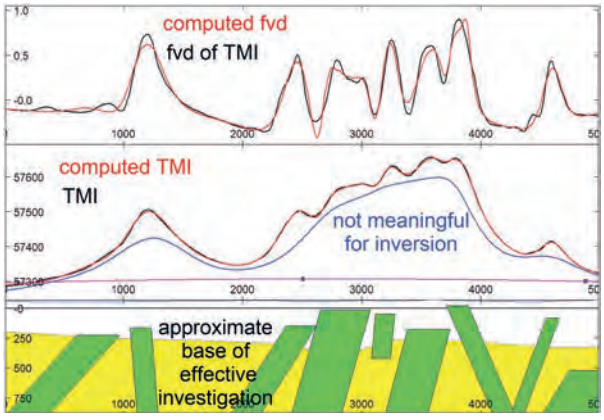

Fig. 2.41. Bottom) Model X-section from TMI inversion. The top of the yellow zone is the approximate limit below which magnetisation does not dominate curvature of the field and therefore is not resolved by inversion. Centre) measured and computed TMI, Top) vertical derivative of measured and computed TMI.

with considerable input from the magnetic field data in Fig. 2.39 but is a simplified synthesis restricted by the limited availability of information from boreholes and outcrop. Multiple, overlapping field variations along the section of flightline modelled in Fig. 2.41 are separated into only the two geological units of the Cambrian Ponto Group and Wonnaminta Formation. Both are described as packages of predominantly quartzo-feldspathic metasandstones and phyllites, differentiated predominantly by the stronger magnetic signature of the Ponto Group compared to the Wonnaminta Formation. Variability in the TMI image suggests that these packages have significant internal petrophysical variation but it is not feasible to map those variations as specific geological units. The magnetic field data can, however, map

contacts across which there is variation in magnetisation and support inversion to estimate apparent susceptibility contrasts, dips of contacts, and at suitable locations, depth to the top of magnetisation.

Figure 2.41 shows a model section of the profile located in Figs 2.39 and 2.40. The objective of this study was to map depth to the top of magnetisation and recover statistics about its distribution such as thicknesses and dips of prominent magnetic units, rather than to build a complete three-dimensional model for which most of the volume is not meaningfully constrained. I positioned nine bodies to match prominent features along the TMI profile and adjusted their position, strike extent and azimuth in map view to match the anomaly extents and orientations. I assumed a horizontal background field, with the bodies explaining all the field variation about an initially unknown base level. Explaining these poorly separated field variations with the minimum number of discrete sources is justified but because the anomalies overlap so strongly any space-filling model of continuous distribution of magnetisation is highly non-unique. The model shown in Fig. 2.41 is also non-unique, but the non-uniqueness has been minimised by focusing on the more reliable features in the field.

The inversion to create the model shown in Fig. 2.41 was permitted to change all model parameters other than northing, strike extent and azimuth, to which there is no sensitivity on the individual profile. The close match of measured and post-inversion model-computed TMI is shown in the centre panel in Fig. 2.41. Typical of least-squares fits to data the most noticeable misfits are rounding of the local maxima and minima. These misfits represent a very small proportion of the data, but unfortunately the part most critical and informative. The top track of Fig. 2.41 shows line-based vertical gradient filters of the measured and model-computed fields which more clearly reveal failings of the model in reproducing the sharpest measured TMI variations.

The sum of the magnetisation in the model matches the measured field variation but there is considerable variation in sensitivity to different parts of the model. The tops of the shallowest bodies are less than 200 m below the measurements and bodies appear to extend more than a kilometre beneath that. The deeper parts of the magnetisation produce small contributions to the magnetic field variations and do not contribute at all to the local field gradients which carry the most diagnostic information. In Fig. 2.41 I have drawn an approximate and indicative surface below which there is little justification to delineate magnetisation. In the model of Fig. 2.41 the deeper magnetisation is produced by the lower segments of the bodies for which the tops at shallow depth match the partially separated sharp field variations. Alternatively, the deeper magnetisations could be replaced across a horizontal discontinuity by any number of different deep magnetisation distributions. In Fig. 2.41 I have also shown the approximate corresponding split between magnetic field contributions from shallow, partially resolved magnetisations and deeper unresolved magnetisations. This twofold classification is a considerable simplification but it is a great improvement on supplying the model of Fig. 2.41 without discrimination between aspects which are reasonably justified and aspects which are not justified at all. Failure to provide at least an indication of this separation both devalues those parts of the model which have some reliability and includes features which might be interpreted but which have no justification.

The upper gradient filter track of Fig. 2.42 highlights the curvature features in the lower TMI track that have been designated as those parts of the field with significance for analysis and interpretation. All the information about magnetisation that can be meaningfully recovered from the inversion has expression in the gradient data, and the gradient data consists mostly of this separation of the field. The bottom track of Fig. 2.42 shows an alternative model from inversion of the gradient filter. Small features are more prominent in the gradient filters than in the field data and I used 14 bodies to match these gradient anomalies compared to nine for the TMI inversion.

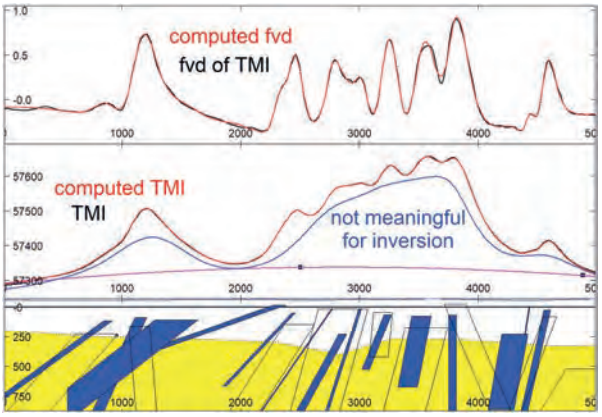

Fig. 2.42. Bottom) Model X-section from inversion of the vertical derivative filter of TMI. The top of the yellow zone is the approximate limit below which magnetisation does not dominate curvature of the field and therefore is not resolved by inversion. Centre) measured and computed TMI; Top) vertical derivative of measured and computed TMI.

Most of the misfit for this vertical derivative inversion (just as for the previous TMI inversion) is in rounding local maxima and minima. However, because the inversion focuses on matching this small part of the field, it matches those gradients much more closely than is achieved by the TMI inversion of Fig. 2.41. For the more sharply defined anomalies depths to the top of magnetisation are reasonably consistent between the TMI and vertical gradient inversions. Focus on the short wavelength magnetic variations using the gradient data necessarily reduces sensitivity to the longer wavelength variations. However, having matched the gradient filters in the top track of Fig. 2.36, that model can be subsequently inverted to best fit the TMI data by changing only the depth extent of the bodies and the regional field. This second-stage inversion does not significantly disrupt the already achieved fit of the gradients.

There is a further selective optimisation in terms of results obtained for effort spent. In this study I have run a single profile inversion. The model is simple (nine individual and independent bodies for the TMI inversion and 14 for the vertical gradient inversion) and the number of data points is small (600) so that inversions run very quickly even with many iterations. The final models are easily summarised in a set of data points which contain statistics for each model body such as depth to top, apparent susceptibility, width, azimuth and dip. Inclusion of the vertical gradient inversion increases the time spent but improves efficiency in recovering reliable results. A full three-dimensional volume inversion would take longer, be less interactive, and would not necessarily provide any additional reliable information. Information from the few-body profile inversion is concisely condensed and easily imported to GIS packages for integration with other information. The location of the profile can be selected from inspection of the field data to ensure that the most significant field variations are sampled and having completed one profile inversion, the decision can be made about how far to step to the next one. This process gives a versatile focus on the most informative field variations across the area or those most relevant to specific exploration objectives.

REFERENCES

Alavi SN (2013) 'Structure, stratigraphy, and petroleum prospectivity of the Waukarlycarly Embayment, Canning Basin, Western Australia'. Record 2013/10. Geological Survey of Western Australia, Perth.

Blake DH, Horsfall CL (1986) 'Elkedra Region, Northern Territory (First Edition). 1:100 000 geological map commentary, parts of 5955, 5855 and 6055'. Bureau of Mineral Resources, Australia, Canberra.

Blakely RJ (1995) 'Potential theory in gravity and magnetic applications'. (Cambridge University Press)

Briggs IC (1974) Machine contouring using minimum curvature. *Geophysics* **39**, 39–48. doi:10.1190/1.1440410

Chwala A, Stolz R, Zakosarenko V, Fritzsch L, Schulz M, Rompel A, Polome L, Meyer M, Meyer HD (2012) Full Tensor SQUID Gradiometer for airborne exploration. *ASEG Extended Abstracts* **2012**(1), 1–4. doi:10.1071/ASEG2012ab296

Davis A (2022) Nested anisotropic geostatistical gridding of airborne geophysical data. *Geophysics* **87**, E1–E12. doi:10.1190/geo2021-0169.1

Foss CA, Purcell PG (2006) Structure and hydrocarbon prospectivity of the Waukarlycarly graben, West Australia in 'Abstracts: American Association of Petroleum Geologists; AAPG International Conference and Exhibition'. (AAPG: Perth, Western Australia).

Foss CA, Gouthas G, Wilson TC, Katona LF, Heath P (2019) Gawler Craton Airborne Geophysical Survey, Region 9A, Childara – enhanced geophysical imagery and magnetic source depth models Report Book 2019/00008. Department for Energy and Mining, South Australia, Adelaide.

Hegarty RA (2017) 'Cobham Lake 1: 250 000 Geophysical-Geological Interpretation Map'. Sheet SH/54–11. (Geological Survey of New South Wales, Maitland)

Hood PJ, Teskey DJ (1989) Aeromagnetic gradiometer program of the Geological Survey of Canada. *Geophysics* **54**, 1012–1022. doi:10.1190/1.1442726

Isles DJ, Rankin LR (2013) 'Geological Interpretation of Geological Data.' (Australian Society of Exploration Geophysics)

Katona LF, Reed GD, Heath PJ (2021) 'The Gawler Craton Airborne Survey, 2017 – 2021: Final Report, Report Book 2021/00017.' Department for Energy and Mining, South Australia, Adelaide.

Li Y, Oldenburg DW (1998) Separation of regional and residual magnetic field data. *Geophysics* **63**, 431–439. doi:10.1190/1.1444343

Miller HG, Singh V (1994) Potential field tilt - a new concept for location of potential field sources. *Journal of Applied Geophysics* **32**, 213–217. doi:10.1016/0926-9851(94)90022-1

Minty BRS (1991) Simple micro-levelling for aeromagnetic data. *Exploration Geophysics* **22**, 591–592. doi:10.1071/EG991591

Naprstek T, Smith RS (2019) A new method for interpolating linear features in aeromagnetic data. *Geophysics* **84**, JM15–JM24. doi:10.1190/geo2018-0156.1

Naudy H (1971) Automatic determination of depth on aeromagnetic profiles. *Geophysics* **36**, 717–772. doi:10.1190/1.1440207

Pawley M, Irvine J, Melville A, Krapf C, Thiel S, Gonzale-Alvarez I, Kelka U, Martinez C (2021) Automated lineament analysis of the Gairdner Dolerite dyke swarm of the Gawler Craton. *MESA Journal* **95**, 30–40.

Reeves C (2005) Aeromagnetic surveys: Principles, practice and interpretation. Earth-works, Washington DC, 155 p.

Reid AB (1980) Aeromagnetic survey design. *Geophysics* **45**, 895–982. doi:10.1190/1.1441102

Schmidt PH, Clark DA, Leslie KE, Bick M, Tilbrook D, Foley C (2004) GETMAG – a SQUID magnetic tensor gradiometer for mineral and oil exploration. *Exploration Geophysics* **35**, 297–305. doi:10.1071/EG04297

Shi Z (1991) An improved Naudy-based technique for estimating depth from magnetic profiles. *Exploration Geophysics* **22**, 357–362. doi:10.1071/EG991357

Shi Z, Boyd D (1993) AUTOMAG - An automatic method to estimate thickness of overburden from aeromagnetic profiles. *Exploration Geophysics* **24**, 789–794. doi:10.1071/EG993789